Chapter 3

Experimental overview

As discussed in Chapter 2, one of the promising candidate platforms to realize strong atom-photon coupling is microtoroidal resonator based cavity QED systems. As the first on-chip monolithic lithographically fabricated platform that achieved strong atom-photon coupling, investigations on this platform where atoms interact with evanescent fields at the nano-scale (~ 100 nm) are interesting not only in their own right but also in revealing the physical factors or elements important in this world of nanophotonic atom-photon interaction, including: the role of dielectric surfaces in modifying atomic internal electronic states and decay rates, the center-of-mass dynamics of single atoms near dielectric surfaces, the electric field polarization behavior of strongly confined light at sub-wavelength scales and its role in atom-photon interactions, and the critical aspects of nanophotonic device fabrication in the context of atom-photon interactions. While some of these issues were investigated in microtoroidal-based cavity QED experiments conducted in this thesis (Chapters 4, 5, 6), some of the latter issues were investigated in more detail in an optical nanofiber platform (Chapter 7). As discussed in more detail in later sections and chapters of this thesis, these cavity QED systems demand strict and high quality photonic device fabrications, which are critical and may limit the performance or even function of the system, such as the ability to trap single atoms. With the combined knowledge of experimental investigations on microtoroidal resonator and optical nanofiber, we investigate a cavity QED platform based on lithographically fabricated nanophotonic waveguides and photonic crystal resonators (Chapter 8), which hold bright promise towards the realization of a chip-integrated scalable quantum network with strong coupling of trapped single atoms to single photons with $N \gg 1$ number of nodes, allowing multiple qubit operations in quantum computation contexts, as well as quantum simulations of many-body systems represented by the atoms.

In this chapter, we present basic experimental setups of this thesis, the basic experimental techniques involved, and explore the three types of nanophotonic devices considered in this thesis,

namely: microtoroid cavity QED (Sec. 3.1), tapered optical nanofiber (Sec. 3.2), and nanophotonic waveguides and cavities (Sec. 3.3).

3.1 Cavity QED with a microtoroidal cavity

3.1.1 Model

3.1.1.1 Modes of a microtoroidal resonator

An idealized microtoroid has axial symmetry, so we work in a standard cylindrical coordinate system $\vec{r} \to (\rho, \phi, z)$. The toroid is modeled as a circle of diameter D_{m} with dielectric constant ϵ revolved around the z-axis to make a torus of major diameter D_{M} (Fig. 3.1 (a)). The toroid is therefore defined by its minor diameter D_{m} and its principal diameter $D_{\mathrm{p}} = D_{\mathrm{M}} + D_{\mathrm{m}}$. The fabrication and characterization of high-quality microtoroids are described in detail elsewhere [11].

The axisymmetric cavity modes of interest are whispering-gallery modes (WGM), which lie near the edge of the resonator surface and circulate in either a clockwise or counter-clockwise direction. These modes are characterized by an azimuthal mode number m, whose magnitude gives the periodicity around the toroid and whose sign indicates the direction of propagation. The WGMs for $\pm m$ are degenerate in frequency but travel around the toroid in opposite directions. The mode electric fields for the WGM traveling waves are written as $\vec{E}(\vec{r}) = E_{\max}\vec{f}(\rho, z)e^{im\phi}$, where $\vec{f}(\rho, z) = \vec{E}(\rho, z)/E_{\max}$ is the mode function in the $\rho - z$ cross-section normalized by the maximum electric field $E_{\max}$. In general, backscattering couples these two modes so that a more useful eigenbasis for the system consists of the normal, standing wave modes characterized by a phase and the periodicity $|m|$. This backscattering coupling h is assumed to be real, with the phase absorbed into the definition of the origin of the coordinate ϕ. In addition, the mode's field decays at a rate κ_{i} through radiation, scattering, and absorption. In our simulations, a cavity mode is fully described by its spatial mode function $\vec{f}(\vec{r})$, its azimuthal mode number m, its loss rate κ_{i}, and the coupling h to the counter-propagating mode with mode number $-m$.

We model the microtoroid modes using a commercial finite-element software package (COMSOL) to solve numerically for the vector mode functions $\vec{f}(\rho, z)$ for modes of a given m [180]. Mode volumes are calculated from,

$$V_{\mathrm{m}} = \frac{\int dV\, \epsilon(\vec{r})|\vec{E}(\vec{r})|^2}{E_{\max}^2} = 2\pi \int dA\, \epsilon(\rho, z)\rho f(\rho, z)^2. \tag{3.1}$$

In this notation [224], the coupling of a circularly polarized optical field to an atomic dipole located

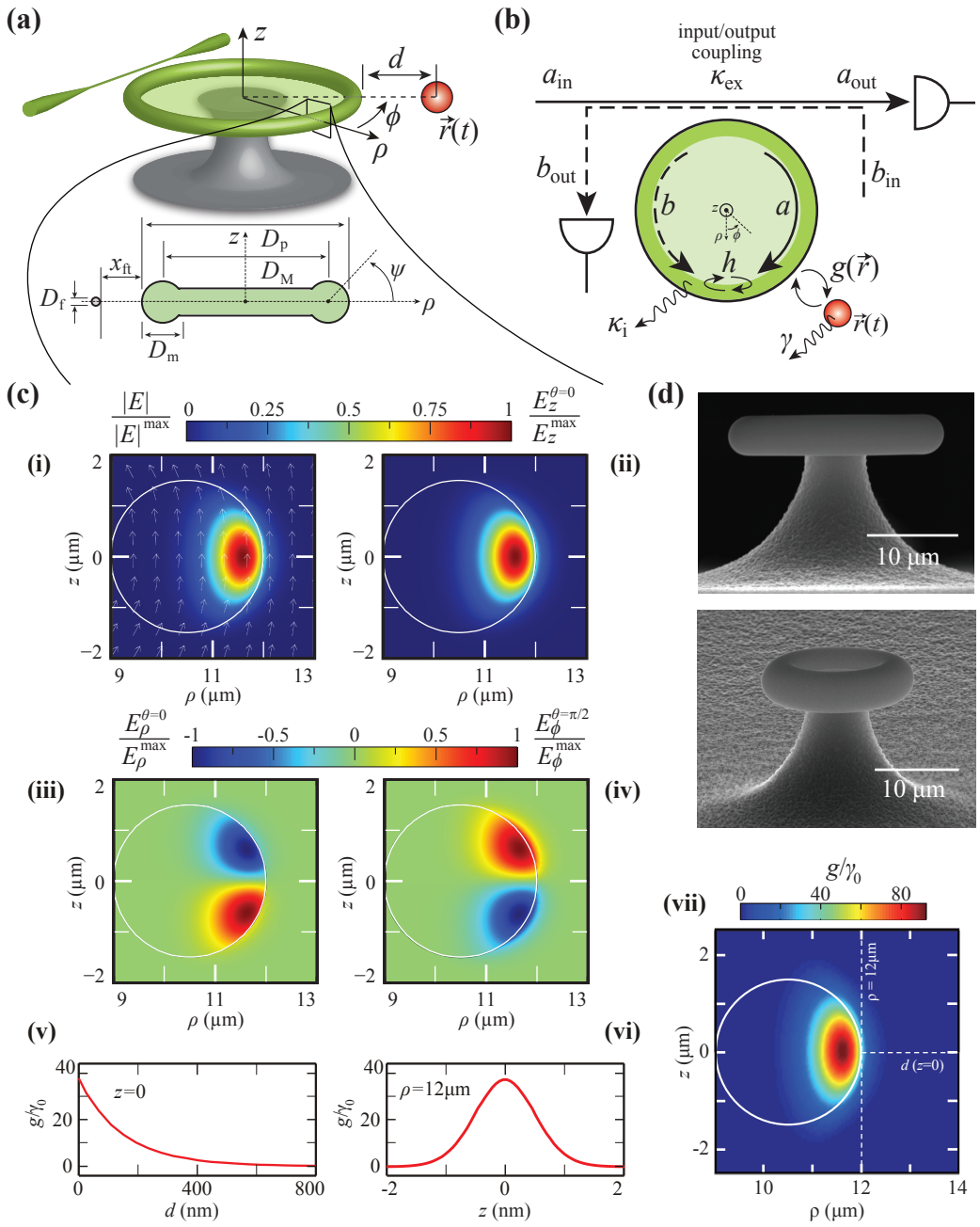

Figure 3.1: **Microtoroid cavity QED schematic.** **(a)** Optical input/output coupling enabled by a tapered fiber (diameter D_{f}) positioned at a small fiber/toroid surface-to-surface gap $x_{\mathrm{ft}} < \lambda$. Spatial cylindrical coordinates $\{\rho, \phi, z\}$ with origin at toroid center. The toroid geometry can be described by its major (D_{M}), minor (D_{m}), and principal (D_{p}) diameters. On the toroid's cross-sectional minor circle plane, ψ describes the latitudinal angle, and $d = d(\rho, z)$ is the atom-to-surface distance. **(b)** Tapered fiber optical input/output fields $\{a_{\mathrm{in}}, a_{\mathrm{out}}, b_{\mathrm{in}}, b_{\mathrm{out}}\}$ coupled at rate κ_{ex} to toroid counter-propagating intracavity fields $\{a, b\}$, coupled by internal scatterers at a rate h, suffering intrinsic loss at rate κ_{i}. A nearby atom located at $\vec{r}$ is coupled to the cavity at rate $g(\vec{r})$, and has a free space spontaneous emission rate γ. **(c)** i-iv): normalized electric field $|E|$ profiles and the components $\{E_z^{\theta}, E_\rho^{\theta}, E_\phi^{\theta}\}$ (where θ indicates the optical phase), with $E_z^{\max} = 1.00|E|^{\max}, E_\rho^{\max} = 0.086|E|^{\max}, E_\phi^{\max} = 0.118|E|^{\max}$; v-vii) shows the lowest-order mode function $f(\rho, z)$ for a toroid with $\{D_{\mathrm{p}}, D_{\mathrm{m}}\} = \{24{,}3\}$ μm, $m = 118$ and $\lambda = 852$ nm, and the cross-sections along d and z. **(d)** SEM images of two fabricated mictoroids with $D_{\mathrm{p}} \sim 18$ μm and $D_{\mathrm{p}} \sim 24$ μm.

in the evanescent field of the cavity is calculated as:

$$g(\vec{r}) = \langle \vec{d} \cdot \vec{E} \rangle = f(\rho, z) e^{im\phi} \sqrt{\frac{3\pi c^3 \gamma}{{\omega_{\rm a}^{(0)}}^2 V_{\rm m}}}, \tag{3.2}$$

where $\vec{d}$ is the dipole operator and $\omega_{\rm a}^{(0)} = 2\pi c/\lambda_0$ is the vacuum transition frequency of the two-level atom with free-space wavelength λ_0. WGMs are predominantly linearly polarized, and so we average over the dipole matrix elements to obtain an effective traveling wave coupling $g_{\rm tw}$ which is approximately ~ 0.6 of the value for circularly polarized light (see supplementary information of [9]). Travelling wave modes of an axisymmetric resonator are not strictly transverse. For the toroid geometries considered here, with $D_{\rm p}, D_{\rm m} \gg \lambda$, the azimuthal component is small and we assume that the optical field is linear outside of the toroid. Since the cavity losses are dominated by absorption and defect scattering rather than the radiative lifetime set by the toroid geometry [224], we let $\kappa_{\rm i}$ and h be experimental parameters. Fig. 3.1 (c) shows SEM images of two fabricated mictoroids with $D_{\rm p} \sim 18$ μm and $D_{\rm p} \sim 24$ μm, and the lowest-order mode with $m = 118$ for a toroid with $\{D_{\rm p}, D_{\rm m}\} = \{24, 3\}$ μm. The index m is chosen so that the cavity frequency $\omega_{\rm c}$ is near the $6S_{1/2} \rightarrow 6P_{3/2}$ transition of Cs with $\omega_{\rm a}^{(0)}/2\pi = 351.7$ THz.

The local polarization of modes varies throughout the interior and exterior of the toroid. Approximate solutions for constant polarization suggest classifications as quasi-transverse modes, labeled transverse electric (TE) and transverse magnetic (TM) modes, although actual solutions are not transverse. A reasonable analytic approximation for the lowest-order mode function with mode number m outside of the toroid is that of a Gaussian wrapped around the toroid's surface that decays exponentially with the distance scale set by the free space wavevector $1/\lambda\!\!\!^{-}_0 = 2\pi/\lambda_0$,

$$f(\rho, z) \sim e^{-d/\lambda\!\!\!^{-}_0} e^{-(\psi/\psi_0)^2}, \tag{3.3}$$

where $d(\rho, z) = \sqrt{(\rho - \frac{D_{\rm M}}{2})^2 + z^2} - \frac{D_{\rm m}}{2}$ is the distance to the toroid surface, $\psi(\rho, z) = \arctan \frac{z}{\rho - D_{\rm M}/2}$ is the angle around the toroid cross-section ($\psi = 0$ at $z = 0$), and ψ_0 is a characteristic mode width (see Fig. 3.1 (a)). Higher order angular modes are characterized by additional nodes along the coordinate ψ.

3.1.1.2 Fiber-toroid optical coupling

As discussed in previous sections, we couple light into and out of the microtoroidal cavity using a tapered optical nanofiber. In this section we consider in more detail this coupling between the

two photonic modes. As will be discussed in more detail in Chapter 6, another potential function for the nanofiber is to provide trapping of single atoms, which could potentially realize strong coupling between trapped atoms and photons using a microtoroid platform. With this context in mind, we now proceed to take a look at how the toroid-fiber coupling can be modelled, and importantly its behavior as a function of varying the toroid's dimensions (hence its propagation constant), nanofiber dimensions (hence its propagation constant), and the fiber-to-toroid spacing. In the experiment, we tune the fiber-to-toroid spacing (x_{ft}) by using nanopositioners, which allow tuning of the input/output coupling rate κ_{ex}, allowing access to under-coupled ($\kappa_{\mathrm{ex}} < \sqrt{\kappa_{\mathrm{i}}^2 + h^2}$), critically coupled ($\kappa_{\mathrm{ex}} = \sqrt{\kappa_{\mathrm{i}}^2 + h^2}$), and over-coupled ($\kappa_{\mathrm{ex}} > \sqrt{\kappa_{\mathrm{i}}^2 + h^2}$) regimes. We note that depending on the phase-matching conditions (dimensions and materials of the toroid and fiber), it is possible for critical-coupling (and hence also over-coupling) conditions to be unattainable even when the fiber-to-toroid gap is zero (i.e., the fiber is in contact with the toroid).

As illustrated in Figure 3.2 a), we model our toroid and fiber as two parallel cylindrical waveguides, with a surface-to-surface gap of x_{ft}, interaction length of L_{ft}, nanofiber radius of a, and toroid principal radius r_{p}. We note that, as we will discuss later, the minimum range of L_{ft} for our typical parameters that may lead to a maximum transfer of power between one initially excited waveguide to the other (initially not excited) waveguide is in the order of $\sim 1\ \mu m$. Given the typical sizes of the toroid (e.g., diameter of 20-50 μm), the curvature in the $\sim 1\mu$m scale should be relatively small, and the assumption of two parallel cylindrical waveguides is reasonable. A more precise model should take into account the curvature of the toroid as we move along the z-axis, instead of assuming two parallel waveguides with an effective interaction length of L_{ft} that we use here.

Our model is based on the coupled mode theory of two parallel waveguides discussed in [257]. The dispersion curves showing the two lowest order 'supermodes' of a pair of waveguides (labeled waveguides a and b) with configuration near the phase-matching frequency ω_0 is illustrated in Fig. 3.2 c). Here, as we approach ω_0, the individually uncoupled waveguide dispersion curves $\beta'_{\mathrm{a}}(\omega)$ and $\beta'_{\mathrm{b}}(\omega)$ exhibit anti-crossing near the phase-matching frequency, and the supermodes are described by the dispersion curves $\gamma_1(\omega)$ and $\gamma_2(\omega)$ for the odd and even modes respectively. One parameter that affects the strength of the coupling between the two waveguides is the phase-matching coefficient, δ.

Consider the initial condition where light is initially injected only into waveguide b, with power $P_{\mathrm{b}} = P_0$; and no light is travelling through waveguide a. Let us assume that this initial condition is satisfied at $z = 0$. The power transferred to waveguide a, as a function of the interaction length, z,

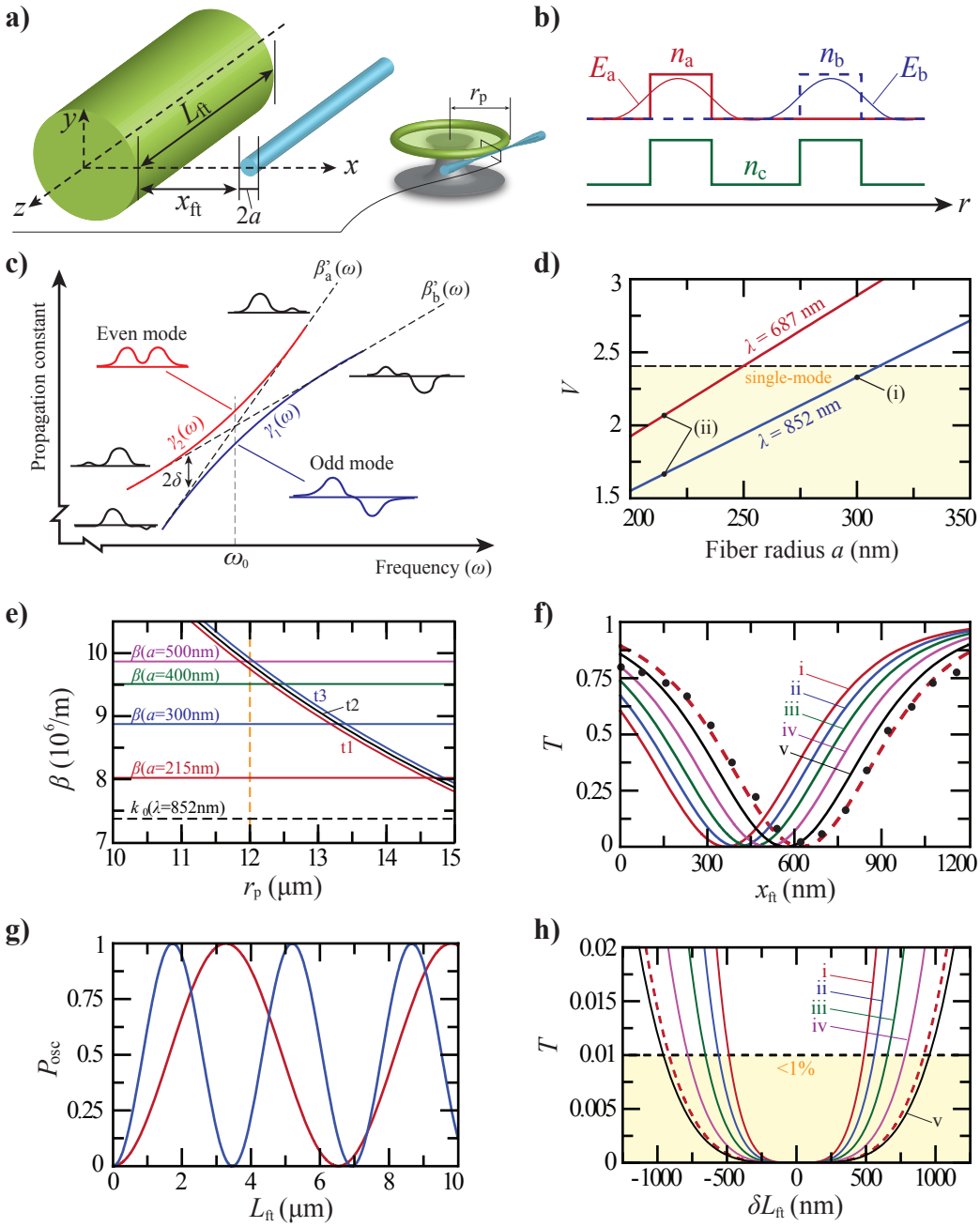

Figure 3.2: **Microtoroid-nanofiber optical coupling. a)** Nanofiber (radius a) and microtoroidal cavity (principal radius r_p, minor radius $r_\mathrm{m} = 1.5$ μm) interacting over an effective interaction length L_ft, with gap x_ft, modeled as two parallel cylindrical waveguides. **b)** Transverse cross-section of a pair of generic waveguides (a, b), with electric fields $(E_\mathrm{a}, E_\mathrm{b})$, individual (one waveguide) refractive index profiles $(n_\mathrm{a}, n_\mathrm{b})$, and composite (two waveguides) refractive index profile n_c, along a spatial coordinate r. **c)** Dispersion curves near phase-matching frequency ω_0; $\beta_\mathrm{a}, \beta_\mathrm{b}$: no coupling; γ_1, γ_2: lowest order odd and even supermodes; δ: phase-matching coefficient. **d)** Fiber V-parameter, $V = ka\sqrt{n^2 - n_\mathrm{air}^2}$, where $k = 2\pi/\lambda$, $n = 1.452$ (SiO_2), $n_\mathrm{air} = 1$; (i) fiber radius $a \simeq 300$ nm, (ii) $a = 215$ nm; single-mode ($V < 2.405$) shaded. **e,f,h)** Curves i-v: fiber radius $a = 215$ nm and toroid principal diameter $D_\mathrm{p} = 12$, 12.3, 12.6, 12.9, 13.2 μm (dashed red curves: $a = 300$ nm, $D_\mathrm{p} = 12$ μm). **e)** t1, t2, t3: toroid whispering-gallery-mode with azimuthal mode numbers 117, 118, 119 respectively, $k_0 = 2\pi/\lambda$, $\lambda = 852$ nm. **f)** Transmittance T (x_ft is fiber-toroid gap). **g)** Oscillatory term P_osc of fiber-toroid coupling strength (fiber radius 215 nm (blue), 300 nm (red)). **h)** Transmittance T vs δL_ft, the deviation from L_ft value that maximizes P_osc, at critical coupling.

is then given by [257]:

$$P_{\mathrm{a}}(z) = P_0 P_{\mathrm{frac}} P_{\mathrm{osc}} = P_0 \frac{\kappa^2}{\kappa^2 + \delta^2} \sin\left(\left(\sqrt{\kappa^2 + \delta^2}\right) z\right), \tag{3.4}$$

where $P_{\mathrm{b}} = P_0 - P_{\mathrm{a}}(z)$ is the power in waveguide b for the given z. The term $P_{\mathrm{frac}} = \frac{\kappa^2}{\kappa^2+\delta^2}$ determines the maximum possible fraction of power transfer and the term $P_{\mathrm{osc}} = \sin\left(\left(\sqrt{\kappa^2 + \delta^2}\right) z\right)$ is oscillatory as a function of the coupling length z (or L_{ft}). The phase-matching coefficient δ is given by:

$$\delta = \frac{1}{2}\left((\beta_{\mathrm{b}} + M_{\mathrm{b}}) - (\beta_{\mathrm{a}} + M_{\mathrm{a}})\right), \tag{3.5}$$

where β_{a} and β_{b} are the propagation constants of waveguides a and b respectively, whereas M_{a} and M_{b} are small correction terms to the waveguides' a and b propagation constants respectively, due to the presence of the other waveguide, and are given by

$$M_i = \frac{\omega\epsilon_0}{4} \int_{-\infty}^{\infty} (n_i^2(r) - n_{\mathrm{c}}^2(r)) E_i^2 \mathrm{d}A, \tag{3.6}$$

where i denotes the waveguide label (i.e., a or b), ϵ_0 is the vacuum permittivity constant, $n_i(r)$ is the refractive index profile for waveguide i only (in the absence of the other waveguide) as a function of spatial coordinate r, $n_{\mathrm{c}}(r)$ is the composite (two waveguides, both a and b present) refractive index profile (see Fig. 3.2 b)), and E_i is the unperturbed electric field for waveguide i. Finally, the effective coupling constant κ is given by the geometric mean of the coupling constant for waveguides (a to b) and (b to a) [257, 222], $\kappa = \sqrt{\kappa_{\mathrm{ab}}\kappa_{\mathrm{ba}}}$, where

$$\kappa_{ij} = \frac{\omega\epsilon_0}{4} \int_{-\infty}^{\infty} (n_i^2(r) - n_{\mathrm{c}}^2(r)) E_i E_j \mathrm{d}A. \tag{3.7}$$

We note that given the above equations,

$$\kappa = \sqrt{\kappa_{\mathrm{ab}}\kappa_{\mathrm{ba}}} = \sqrt{n_{\mathrm{b}}^2 n_{\mathrm{a}}^2} \frac{\omega\epsilon_0}{4} \int_{-\infty}^{\infty} E_{\mathrm{a}} E_{\mathrm{b}} \mathrm{d}A = \beta_{\mathrm{a}}\beta_{\mathrm{b}} C_0, \tag{3.8}$$

where C_0 is a proportionality constant that contains in it the integral involving the electric field profiles of the waveguides. Note that we have used $n_i = \beta_i/k_0$ with $k_0 = \frac{2\pi}{\lambda}$, the free-space wave number. At this point, we make an approximation to treat the value C_0 to be constant, as we modify the dimensions at the toroid and fiber in the discussions that follow. This approximation is based on the assumption that the taper-toroid coupling strength is most sensitive to the phase-matching

conditions determined by the propagation constants, and the value of the integral inside C_0 does not change significantly relative to these changes.

We now find the propagation constants of the microtoroid whispering gallery mode and the nanofiber. For the microtoroid, the intrinsic propagation constant is given by $\beta_{\text{toroid}} = 2\pi/\lambda_{\text{eff}} = 2\pi/(2\pi r_{\text{eff}}/m) = m/r_{\text{eff}} \approx m/r_{\text{p}}$ where m is the azimuthal mode number and r_{eff} is the effective toroid mode radius and r_{p} is the principal radius [222]. In our calculation, we use the principal radius for the toroid used in the experiment discussed in Chapter 5, $r_{\text{p}} = 12$ μm, and the azimuthal mode number m=118, which brings the toroid's resonant frequency to that of the cesium D2 ($F = 4 \rightarrow F' = 5$ transition) at $\lambda \approx 852$ nm. To see the sensitivity to changes in m, in Fig. 3.2 e), we plot the propagation constant β_{toroid} as a function of r_{p} for $m = 117, 118, 119$ (labeled t1, t2, t3) in red, black, and blue respectively. The propagation constants for the nanofiber can be calculated analytically or by using COMSOL (see Sec. 3.2). In Fig. 3.2 e), we include the propagation constants for nanofiber of radii $a = 215, 300, 400, 500$ nm, as well as the free-space wave number $k_0 = 2\pi/\lambda_0$ with $\lambda_0 = 852$ nm. We note that in the toroid cavity QED experiments described in Chapter 4 and Chapter 5, we used a nanofiber with estimated radius $a = 300$ nm, pulled from a single-mode fiber SM800 from Fibercore. In the nanofiber atom trap experiment described in Chapter 7, we used a nanofiber with estimated radius $a = 215$ nm, pulled from a single-mode fiber 630-HP from Nufern. We also consider use of this smaller final radius fiber $a = 215$ nm for the atom trap scheme using a tapered nanofiber next to a microtoroid described in Chapter 6. One of the main reasons is the requirement to have the nanofiber to support only a single-mode at the cesium D2 line magic wavelengths 687 nm and 937 nm (used for the blue-detuned and red-detuned trapping beams, respectively), and the probe light at 852 nm. While the larger nanofiber ($a = 300$ nm) is single-mode for 852 nm and 937 nm, it is not single-mode at 687 nm. This is illustrated in Fig. 3.2 d) where point (i) indicates single-mode condition for $\lambda = 852$ nm but not 687 nm, and points (ii) indicate the single-mode condition for $\lambda = 687$ nm and 852 nm. The shaded region indicates the single-mode region with $V < 2.405$.

Now, two measureable quantities in the experiment are the power of the input light into the fiber, P_{in}, and the transmitted power coming out of the fiber, P_{T} after it interacts with the microtoroid cavity, leading to the transmittance $T = P_{\text{T}}/P_{\text{in}}$. As a function of the so-called coupling factor K, the transmission is given by [222]:

$$T(K) = \left(\frac{1-K}{1+K}\right)^2, \tag{3.9}$$

where

$$K = \frac{\kappa_0^2 e^{-\gamma_0' x_{\text{ft}}}}{\kappa_{\text{i}}^2 e^{-\gamma_{\text{i}}' x_{\text{ft}}} + (\sigma_0')^2}. \tag{3.10}$$

Here K is the ratio of desired nanofiber-toroid mode power coupling to the total power loss of the system, $x_{\rm ft}$ is the fiber-toroid surface-to-surface distance, κ_0 is the coupling constant into the fundamental nanofiber mode, $\kappa_{\rm i}$ is the coupling constant into the higher-order (lossy) nanofiber modes, $1/\gamma_0'$ and $1/\gamma_{\rm i}'$ are spatial exponential decay constants associated with the evanescent fields of the fundamental and higher-order nanofiber modes (not to be confused with spontaneous decay rates that use similar symbols in this thesis), and σ_0' is the microtoroid resonator loss rate constant (not to be confused with atomic scattering cross-section). We note that the units of $\kappa_0^2, \kappa_{\rm i}^2$ and σ_0^2 are all 1/sec, representing coupling (loss) rates per second. In our calculation, we use the values $1/\gamma_0' = 1/\gamma_{\rm i}' = 174$ nm, which represent the $1/e$ spatial exponential decay constant for the nanofiber modes, and $\sigma_0 = \sqrt{\frac{2\pi c}{\lambda Q_{\rm i}}}$ with $\lambda = 852$ nm; c the speed of light in vacuum; and $Q_{\rm i} = 5 \times 10^7$, the intrinsic quality factor of the toroid, corresponding to the experimental parameters of Chapter 5.

Our first goal now is to apply our model to our experimental measurement data of transmission T as a function of $x_{\rm ft}$ that were taken in the experiment described in Chapter 5 by tuning the relative position between our toroid and nanofiber using an independently calibrated nanopositioner (see Appendix A). Recall that here the nanofiber radius is $a = 300$ nm. The experimental data is shown in Fig. 3.2 f) as the black points. Using the equations and parameters presented above, one can compute the transmission T as a function of $x_{\rm ft}$, given the two values of $\kappa_{\rm i}$ and κ_0. The value of $\kappa_{\rm i}$ determines the ratio of the values of T at the far under-coupled position to the highly over-coupled position. Independent investigations show that this is typically very small and the fiber-toroid coupling efficiency can be as high as 99.97% [223]. We note that below certain values of $\kappa_{\rm i}$, the shape of T becomes insensitive to the exact value of $\kappa_{\rm i}$. For our calculation, we set $\kappa_{\rm i} = 10^3$ such that $\kappa_{\rm i}^2/\kappa_0^2 < 0.001$. This leaves us with one free parameter, κ_0, which in principle can be calculated from the exact field distributions of the toroid and nanofiber, taking into account the effects due to the various curvatures and also experimental uncertainties. In our calculation, instead of modeling this part of the equation to compute κ_0, we set κ_0 to be fitted by the experimental data[1]. Specifically, we set $\kappa_0 = 4 \times 10^4$, which leads to a critical coupling condition for the (a=300nm) fiber at $x_{\rm ft} = 600$ nm. Note that the minimum point (the critical coupling condition point) of the transmission curve T is quite sensitive to the value of κ_0, which shifts T horizontally along $x_{\rm ft}$.

Recall in Equation (3.4) the term $\frac{\kappa^2}{\kappa^2+\delta^2}$ determines the maximum fraction of power to be transferred from one waveguide to the other waveguide. From our earlier discussions, we have sufficient information to compute κ and δ for different fiber and toroid dimensions within our model and approximations. We thus apply this to the coupling factor K in Eq. (3.9), that is,

[1] A more detailed modeling of a nanofiber-microsphere coupling system can be found in [152].

$\tilde{K} = K \times \left(\frac{\tilde{\kappa}^2}{\tilde{\kappa}^2+\tilde{\delta}^2}\right) / \left(\frac{\kappa^2}{\kappa^2+\delta^2}\right)$, where the variables with tildes correspond to the values for various fiber and toroid dimensions, and the variables without the tildes correspond to K for the case where we have the experimental data. We show the results in Fig. 3.2 f), where the experimental data is shown by the black points, the theoretical results for this case (fiber with radius $a = 300$ nm and toroid principal radius $r_{\mathrm{p}} = 12$ μm) by the red dashed curve, and the curves i, ii, iii, iv, v (in red, blue, green, magenta, black respectively) are the results for a fiber with radius $a = 215$ nm, and toroid principal radii $r_{\mathrm{p}} = 12$, 12.3, 12.6, 12.9, 13.2 μm respectively.

Lastly, we take a look at the oscillatory term $T_{\mathrm{osc}} \equiv \sin\left(\left(\sqrt{\kappa^2+\delta^2}\right) z\right)$ in Eq. (3.4). The results for T_{osc} for a toroid with $r_{\mathrm{p}} = 12$ μm, and nanofibers of radii $a = 215$ nm and 300 nm are shown as the blue and red curves respectively in Fig. 3.2 g).

Now setting x_{ft} to be at the critical coupling condition (i.e., the minima in T in Fig. 3.2 f)), and letting the interaction length L_{ft} vary by the amount δL_{ft} from the length $L_{\mathrm{ft},0}$ that gives the maximum value of T_{osc}, we see how the transmission $T = P_{\mathrm{T}}/P_{\mathrm{in}}$ is affected as we scan the values of δL_{ft}. This is important for the stability of T with respect to variations in L_{ft}. The result for fiber radius $a = 300$ nm and toroid principal radius $r_{\mathrm{p}} = 12$ μm is shown as dashed red curve in Fig. 3.2 h). The results for fiber radius $a = 215$ nm and toroid principal radius $r_{\mathrm{p}} = 12$, 12.3, 12.6, 12.9, 13.2 μm are shown as the solid curves labeled by i, ii, iii, iv, v respectively in (red, blue, green, magenta, black) colors in Fig. 3.2 h). The shaded area in Fig. 3.2 h) corresponds to $T < 1\%$ showing the necessary stability condition of $\delta L_{\mathrm{ft}} \pm 500$ nm to achieve $T < 1\%$ stability at critical coupling. We note that this is a necessary but not necessarily a sufficient condition. There are other factors such as the laser stability and the stability of x_{ft} that may have larger effects on changes in T. We note that in the experiment described in Chapter 5, we have a stability at critical coupling of $T < 1\%$.

3.1.1.3 Cavity QED in an axisymmetric resonator

We consider a quantum model of a two-level atom at position $\vec{r}(t)$ coupled to an axisymmetric resonator shown schematically in Fig. 3.1. The terminology used here follows the supplemental material of [9], [57], and [5], but the general formalism can be found in additional sources (see [225], for example). As described in section 3.1.1.1, an axisymmetric resonator supports two degenerate counter-propagating whispering-gallery modes at resonance frequency ω_{c} to which we associate the annihilation (creation) operators a and b ($a^\dagger$ and $b^\dagger$). Each traveling-wave mode has an intrinsic loss rate, κ_{i}; the modes are coupled via scattering at rate h. External optical access to the cavity

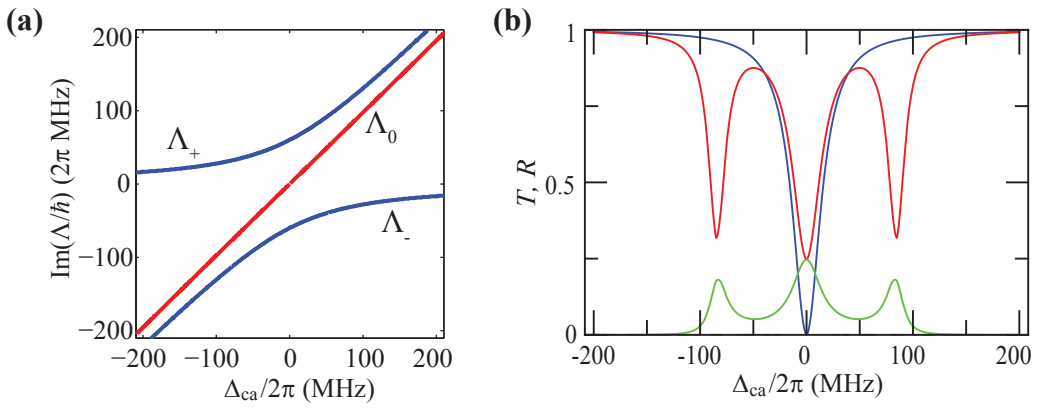

Figure 3.3: **Atom-toroid eigenenergy and spectrum.** **(a)** Imaginary part of the eigenvalues Λ_i of the linearized systems as a function of detuning $\Delta_{\rm ca} = \omega_{\rm c} - \omega_{\rm a}$ for a Cs atom at $\phi = \pi/4$ and $g_{\rm tw}/2\pi = 60$ MHz critically coupled to a cavity with parameters $\{\kappa_{\rm i}, h\}/2\pi = \{8, 0\}$ MHz (Eqs. (3.15)). **(b)** Normalized transmission (red), T, and reflection (green), R, spectra as a function of cavity-atom detuning $\Delta_{\rm ca}$ for $g_{\rm tw} = 0$ and $g_{\rm tw}/2\pi = 60$ MHz ($\theta = \pi/4$) at critical coupling.

is provided by a tapered fiber carrying input fields $\{a_{\rm in}, b_{\rm in}\}$ at probe frequency $\omega_{\rm p}$. Fiber fields couple to the cavity modes with an external coupling rate $\kappa_{\rm ex}$. The output fields of the fiber taper in each direction and are the coherent sum of the input field and the leaking cavity field, $\{a_{\rm out}, b_{\rm out}\} = -\{a_{\rm in}, b_{\rm in}\} + \sqrt{2\kappa_{\rm ex}}\{a, b\}$ [9, 57].

We specialize to the situation of single-sided excitation, where $\langle b_{\rm in}\rangle = 0$. The input field $a_{\rm in}$ drives the a mode with strength $\varepsilon_{\rm p} = i\sqrt{2\kappa_{\rm ex}}\langle a_{\rm in}\rangle$ so that the incident photon flux is $P_{\rm in} = \langle a_{\rm in}^\dagger a_{\rm in}\rangle = |\varepsilon_{\rm p}|^2/2\kappa_{\rm ex}$. Experimentally accessible quantities are the transmitted and reflected photon fluxes, $P_{\rm T} = \langle a_{\rm out}^\dagger a_{\rm out}\rangle$ and $P_{\rm R} = \langle b_{\rm out}^\dagger b_{\rm out}\rangle$, respectively. In experiments, data are typically presented as normalized transmission and reflection coefficients defined as $T = P_{\rm T}/P_{\rm in}$ and $R = P_{\rm R}/P_{\rm in}$. In the absence of an atom, the functions T and R for the bare cavity depend on the detuning $\Delta_{\rm cp} = \omega_{\rm c} - \omega_{\rm p}$ and the cavity rates h, $\kappa_{\rm i}$, and $\kappa_{\rm ex}$. At the critical coupling, $\kappa_{\rm ex} = \sqrt{\kappa_{\rm i}^2 + h^2}$, the bare cavity $T \to 0$ when $\Delta_{\rm cp} = 0$ [223].

The cavity modes $\{a, b\}$ both couple to a single two-level atom with transition frequency $\omega_{\rm a}$ at location $\vec{r}$. In the context of cQED, the atomic system is described by a single transition with frequency $\omega_{\rm a}$ with the associated raising and lowering operators σ^+ and σ^- and an excited state field decay rate γ. The atomic frequency $\omega_{\rm a}(\vec{r})$ may be shifted from the free-space value $\omega_{\rm a}^{(0)}$ by frequency $\delta_{\rm a}(\vec{r})$ due to interactions with the dielectric surface. The coupling of the traveling-wave modes $\{a, b\}$ to the atomic dipole is described by the single-photon coupling rate $g_{\rm tw}(\vec{r}) = g_{\rm tw}^{\rm max} f(\rho, z) {\rm e}^{\pm i\theta}$, where $f(\rho, z)$ is the cavity mode function and $\theta = m\phi$. A discussion of $f(\rho, z)$ for the modes of a microtoroid appears in section 3.1.1.1. For an atom in motion, $\omega_{\rm a}(\vec{r})$, $\gamma(\vec{r})$, and $g_{\rm tw}(\vec{r})$ are spatially-dependent

quantities that depend on the atomic position $\vec{r}(t)$.

To study the atom-cavity dynamics, we write the standard Jaynes-Cummings-style cQED Hamiltonian for coupled field modes [114, 9]:

$$\begin{aligned} H/\hbar = \quad & \omega_{\mathrm{a}}(\vec{r})\sigma^+\sigma^- + \omega_{\mathrm{c}}\left(a^\dagger a + b^\dagger b\right) + h\left(a^\dagger b + b^\dagger a\right) + \left(\varepsilon_{\mathrm{p}}^* e^{i\omega_{\mathrm{p}}t}a + \varepsilon_{\mathrm{p}} e^{-i\omega_{\mathrm{p}}t}a^\dagger\right) \\ & + \left(g_{\mathrm{tw}}^*(\vec{r})a^\dagger\sigma^- + g_{\mathrm{tw}}(\vec{r})\sigma^+ a\right) + \left(g_{\mathrm{tw}}(\vec{r})b^\dagger\sigma^- + g_{\mathrm{tw}}^*(\vec{r})\sigma^+ b\right). \end{aligned} \tag{3.11}$$

Following the rotating-wave approximation, we write the Hamiltonian in a frame rotating at ω_{p} [9, 57, 225]:

$$\begin{aligned} H/\hbar = \quad & \Delta_{\mathrm{ap}}(\vec{r})\sigma^+\sigma^- + \Delta_{\mathrm{cp}}\left(a^\dagger a + b^\dagger b\right) + h\left(a^\dagger b + b^\dagger a\right) + \varepsilon_{\mathrm{p}}^* a + \varepsilon_{\mathrm{p}} a^\dagger \\ & + \left(g_{\mathrm{tw}}^*(\vec{r})a^\dagger\sigma^- + g_{\mathrm{tw}}(\vec{r})\sigma^+ a\right) + \left(g_{\mathrm{tw}}(\vec{r})b^\dagger\sigma^- + g_{\mathrm{tw}}^*(\vec{r})\sigma^+ b\right), \end{aligned} \tag{3.12}$$

where $\Delta_{\mathrm{ap}}(\vec{r}) = \omega_{\mathrm{a}}(\vec{r}) - \omega_{\mathrm{p}}$ and $\Delta_{\mathrm{cp}} = \omega_{\mathrm{c}} - \omega_{\mathrm{p}}$. Dissipation from coupling to external modes is treated using the master equation for the density operator of the system ρ:

$$\begin{aligned} \dot{\rho} = \quad & -\tfrac{i}{\hbar}[H,\rho] + \kappa\left(2a\rho a^\dagger - a^\dagger a\rho - \rho a^\dagger a\right) + \kappa\left(2b\rho b^\dagger - b^\dagger b\rho - \rho b^\dagger b\right) \\ & + \gamma\left(2\sigma^-\rho\sigma^+ - \sigma^+\sigma^-\rho - \rho\sigma^+\sigma^-\right). \end{aligned} \tag{3.13}$$

Here, $\kappa = \kappa_{\mathrm{i}} + \kappa_{\mathrm{ex}}$ is the total field decay rate of each cavity mode, and $2\gamma(\vec{r})$ is the atomic dipole spontaneous emission rate, which is orientation dependent near a dielectric surface (section 6.2.4.1).

The Hamiltonian (3.12) can be rewritten in a standing wave basis using normal modes $A = (a+b)/\sqrt{2}$ and $B = (a-b)/\sqrt{2}$,

$$\begin{aligned} H/\hbar = \quad & \Delta_{\mathrm{ap}}(\vec{r})\sigma^+\sigma^- + (\Delta_{\mathrm{cp}} + h)A^\dagger A + (\Delta_{\mathrm{cp}} - h)B^\dagger B \\ & + \left(\varepsilon_{\mathrm{p}}^* A + \varepsilon_{\mathrm{p}} A^\dagger\right)/\sqrt{2} + \left(\varepsilon_{\mathrm{p}}^* B + \varepsilon_{\mathrm{p}} B^\dagger\right)/\sqrt{2} \\ & + g_{\mathrm{A}}(\vec{r})\left(A^\dagger\sigma^- + \sigma^+ A\right) - i g_{\mathrm{B}}(\vec{r})\left(B^\dagger\sigma^- - \sigma^+ B\right), \end{aligned} \tag{3.14}$$

where $g_{\mathrm{A}}(\vec{r}) = g_{\max} f(\rho,z)\cos\theta$, $g_{\mathrm{B}}(\vec{r}) = g_{\max} f(\rho,z)\sin\theta$, and $g_{\max} = \sqrt{2}g_{\mathrm{tw}}^{\max}$. In the absence of atomic coupling ($g_{\mathrm{tw}} = 0$), these normal modes are eigenstates of (3.12). With $g_{\mathrm{tw}} \neq 0$, the eigenstates of the Hamiltonian are dressed states of atom-cavity excitations. With $h = 0$ and $g_{\mathrm{tw}} \neq 0$, the atom defines a natural basis in which it couples to only a single standing wave mode. For the modes $\{A, B\}$ defined above, coupling may occur predominantly, or even exclusively, to one

of the two normal modes depending the azimuthal coordinate θ. For such θ, the system can be interpreted as an atom coupled to one normal mode in a traditional Jaynes-Cummings model with dressed-state splitting given by the single-photon Rabi frequency $\Omega_{(1)} = 2g \equiv 2g_{\max} f(\rho, z)$, along with a second complementary cavity mode uncoupled to the atom. Approximately for $g_{\rm tw} \gg h$, this interpretation is consistent for any arbitrary atomic coordinate θ. For $h \neq 0$ and comparable to $\kappa_{\rm i}$ with a fixed phase convention (such as $\mathrm{Im}(h) = 0$ used here), this decomposition is not possible for arbitrary atomic coordinate θ; the atom in general couples to both normal modes as a function of ϕ [9, 225].

The master equation (3.13) can be numerically solved using a truncated number state basis for the cavity modes. Alternatively, the system is linearized by treating the atom operators $\sigma^{\pm}$ as approximate bosonic harmonic oscillator operators with $[\sigma^-, \sigma^+] \approx 1$. For a sufficiently weak probe field, the atomic excited state population is small enough that the oscillator has negligible population above the first excited level and the harmonic approximation is quite good. As part of this linearization, we factor expectation values of normally-ordered operator products into products of operator expectation values [66, 80]. Numerical calculations confirm that this approximation is accurate when calculating cavity output fields and classical forces for the weak driving power levels considered here. In particular, experiments typically utilize a photon flux $P_{\rm T} = \langle a^\dagger_{\rm out} a_{\rm out} \rangle \sim 15$ cts/μs corresponding to an average cavity photon population of $\langle a^\dagger a \rangle \sim 0.1$. At these photon numbers, cavity expectation values effectively factorize such that $\langle a^\dagger a \rangle \approx \langle a^\dagger \rangle \langle a \rangle$ for the semiclassical treatment used here [105]. We use this approximation to write $P_{\rm T} = \langle a^\dagger_{\rm out} a_{\rm out} \rangle \approx \langle a^\dagger_{\rm out} \rangle \langle a_{\rm out} \rangle$, implying that we only need the complex number $\langle a_{\rm out} \rangle = -\langle a_{\rm in} \rangle + \sqrt{2\kappa_{\rm ex}} \langle a \rangle$ and its conjugate to calculate the cavity transmission at these photon numbers. This approximation is not sufficient for calculation of the $g^{(2)}(\tau)$ correlation function where the nonlinearities must be included [5], but the linearized two-level atom formalism enables efficient simulation of the behavior of ensembles of atoms at the accuracies required by the existing experimental data in [5].

The relevant equations of motion for the field amplitudes of the linearized master equation are,

$$\langle \dot{a} \rangle = -(\kappa + i\Delta_{\rm cp}) \langle a \rangle - ih \langle b \rangle - i\varepsilon_{\rm p} - ig^*_{\rm tw} \langle \sigma^- \rangle, \tag{3.15}$$

$$\langle \dot{b} \rangle = -(\kappa + i\Delta_{\rm cp}) \langle b \rangle - ih \langle a \rangle - ig_{\rm tw} \langle \sigma^- \rangle, \tag{3.16}$$

$$\langle \dot{\sigma^-} \rangle = -(\gamma + i\Delta_{\rm ap}) \langle \sigma^- \rangle - ig_{\rm tw} \langle a \rangle - ig^*_{\rm tw} \langle b \rangle. \tag{3.17}$$

Time and spectral dependence of this system of equations are governed by its eigenvalues Λ_i. The

imaginary part of the eigenvalues as a function of detuning $\Delta_{\rm ca} \equiv \omega_{\rm c} - \omega_{\rm a}$ are illustrated in Fig. 3.3b. For large $\Delta_{\rm ca} \gg |g_{\rm tw}|$, the three eigenvalues include one atom-like eigenvalue and two cavity-like eigenvalues separated by the mode splitting h. For intermediate $\Delta_{\rm ca}$, there is an anti-crossing of two dressed-state eigenvalues $\Lambda_{\pm}$, while the third (cavity-like) Λ_0 is uncoupled to the atom.

For a slowly-moving atom, the mode fields remain approximately in steady state as the parameters evolve with the atom trajectory $\vec{r}(t)$. Analytic steady-state solutions to (3.15) for $\langle a \rangle_{\rm ss}$ and $\langle b \rangle_{\rm ss}$ are:

$$\langle a \rangle_{\rm ss} = \frac{i\varepsilon_{\rm p}(\gamma+i\Delta_{\rm ap})\left[(\kappa+i\Delta_{\rm cp})(\gamma+i\Delta_{\rm ap})+|g_{\rm tw}|^2\right]}{[ih(\gamma+i\Delta_{\rm ap})+(g_{\rm tw}^*)^2][ih(\gamma+i\Delta_{\rm ap})+g_{\rm tw}^2]-[(\kappa+i\Delta_{\rm cp})(\gamma+i\Delta_{\rm ap})+|g_{\rm tw}|^2]^2}, \tag{3.18}$$

$$\langle b \rangle_{\rm ss} = -\frac{ih(\gamma+i\Delta_{\rm ap})+g_{\rm tw}^2}{(\kappa+i\Delta_{\rm cp})(\gamma+i\Delta_{\rm ap})+|g_{\rm tw}|^2}\langle a \rangle_{\rm ss}, \tag{3.19}$$

$$\langle \sigma^- \rangle_{\rm ss} = -i\frac{g_{\rm tw}\langle a \rangle_{\rm ss}+g_{\rm tw}^*\langle b \rangle_{\rm ss}}{\gamma+i\Delta_{\rm ap}}. \tag{3.20}$$

3.1.2 Experiment setup and techniques

The experiments described in this thesis in Chapters 4 and 5 involving microtoroidal cavities began from an empty table in 2007 shown in Fig. 3.4 e), where some home-built diode lasers were placed inside the safety boxes, along with quadrupole magnetic coils shown on the left, an army of optics at the bottom right side of the table, and then the chambers were baked and pumped by a turbo pump. The setups after the experiments were performed are shown in Fig. 3.4 f-h), where the main chambers are shown in part f), part g) shows the supporting laser sources, optics, and other components for the experiments, and part h) shows two home-built tapered amplifiers on the left and a Ti:Sapph laser on the right used for making the dipole trap conveyor belt.

The realization of and achievements made in the experiments on this microtoroid platform are a result of the close collaboration and hard work of many individuals working on these projects, some of which I would like to especially acknowledge here. Among them are: Prof. Takao Aoki who worked together with me on the project from its inception in 2007, from whom I have learned a great deal, Prof. Scott Parkins of Auckland University, who contributed largely on the underlying theory of our systems, Prof. Nate Stern who made great contributions especially in our atom near surface interaction projects, Dr. Eric Ostby and Dr. Hansuek Lee from the group of Prof. Kerry Vahala who have fabricated the high quality microtoroidal resonators and shared their valuable knowledge. It has been a priviledge to have collaborated with the Vahala group at Caltech, who shared their pioneering expertise especially in optical tapered fiber and microtoroidal resonator systems, central to our experiments. I would also like to acknowledge Prof. Cindy Regal and Prof. Barak Dayan

in our group who have made valuable contributions in these projects based on microtoroidal cavity platform. This work was carried out under the guidance and supervision of my advisor, Prof. Jeff Kimble at Caltech.

The heart of the experiment setup for the microtoroid cavity QED experiments described in Chapters 4 and 5 is shown in Fig. 3.4 a), which consists of two chambers connected by a differential pumping tube, separated by a distance of about 20 cm from the center of the source magneto-optical trap (MOT) chamber on the left, to the center of the science chamber on the right, where the toroid chip is located. This separation is necessary to avoid contamination of the microtoroid chip due to background cesium pressure released by the getter (source), inside the MOT chamber, as well as the large MOT cloud. This makes a significant improvement to the lifetime of the quality factor of the toroids. For example, in the early microtoroid experiment [9], a significant degradation of the toroid's quality factor by more than a factor of two occured as rapidly as within a few months time-scale. In contrast, with the two-chamber setup, the microtoroid's quality factor can be maintained with little degradation for more than a year. We note that the differential pumping tube separating our two chambers is of length a few inches with inner diameter of ≈ 1 cm. While this does not lead to large pressure differential between the two chambers (MOT chamber pressure is $\approx 10^{-9} - 10^{-8}$ torr and science chamber pressure is $\approx 10^{-10} - 10^{-9}$), it is the separation of the microtoroid chip from the Cesium getter and large MOT cloud that is most critical in improving the quality factor lifetime of the microtoroids.

Now, as illustrated in Fig. 3.4 a), a MOT cloud consisting of about 10^9 atoms is created in the MOT chamber, where about 10^8 atoms are then loaded into a one-dimensional optical lattice (standing-wave) FORT trap formed by counter-propagating red-detuned beams whose frequencies are chirped relative to each other, creating a moving optical conveyor-belt, which moves the atom cloud from the MOT chamber to the science chamber 20 cm away. This atom cloud transport takes about 80 ms, resulting in about 10^7 atoms being positioned at about 800 μm on top of the microtoroid chip in the science chamber. These $\approx 10^7$ atoms at a temperature of ≈ 100 μK are then released, where they free-fall down towards a toroid on the chip, which is optically coupled to a tapered nanofiber aligned by stacks of nanopositioners (Attocubes) as shown in Fig. 3.4 a). One in every million of these atoms make its way to a 'good' position about ≈ 100 nm away from the surface of the toroid, and becomes coupled to the single photon cavity mode, leading to optically detectable signals at the output of the single-mode fiber. Using fast programmable electronics (FPGA) in the experiment discussed in Chapter 5, these strongly coupled single atoms can be detected in real-time

in as short as $<$ 500 ns. Given this time reference, one can then make physical changes to the experiments such as the intensity or frequency of the probe laser in the fiber-toroid-atom system using fast switches with a latency of 100-150 ns, and make real-time measurement of these falling single atoms as they couple to the cavity for a transit time of a few μs.

In the subsequent subsections, we discuss in more detail some of the aspects involved in the abovementioned experimental setup, as illustrated in Fig. 3.4.

3.1.2.1 Cold atoms and conveyor belt

As discussed in the previous section, the cold atom cloud preparation starts inside the MOT chamber, where cesium vapor is ejected out of a getter (from SAES, P/N 5G0050, CS/NF/3.9/12 FT10+10) with about 3-5A current running through it. About 10^9 atoms are then collected in a magneto-optical trap formed by three pairs of counter-propagating beams, a quadrupole (anti-Helmholtz) field with ($\approx$ 10 G/cm) that confines the cloud in three dimensions. Each of the six red-detuned (by $\approx$ 12 MHz from cesium D2 line, F=4 $\rightarrow$ F'=5 transition) beams has a power of $\approx$ 5mW with a beam radius of $\approx$ 1 cm, giving an intensity of $I = 1.7$ mW/cm^2 $= 0.62\ I_{\rm sat}$ (total of counter-propagating beams $I = 3.4$ mW/cm^2) where $I_{\rm sat} = 2.71$ mW/cm^2 for isotropic light polarization for the cesium D2 line. The total number of atoms in the MOT of $\approx 10^9$ atoms gives an MOT atom density of $\approx 10^{10}$ atoms/cm^3, and the $1/e$ loading time is about a few seconds. The MOT cloud, with a temperature of about 100 μK, is compressed [58, 99, 255] by changing the beam detuning to -40 MHz (for $\approx$ 10 ms), keeping the repumping beam (F=4 $\rightarrow$ F'=3 transition) constant (with intensity $\approx I_{\rm sat}$), and the cloud is then polarization-gradient cooled by keeping the beam's detuning at -40 MHz, and attenuating the beam's power by $\approx$ 10 dB. We note that the precise values of these numbers are merely a result of optimizations for our specific systems to give the required performance in our experiment. It should be noted that in this specific experiment, as the ultimate goal is to drop the cold atom clouds on top of the toroid, the density of atoms is not something particularly critical, and this can be further improved. Note that in the experiment involving nanofiber and nanophotonic beams, where we overlap a magneto-optically trapped and cooled atom cloud with the nanophotonic device, the atom density number is actually one of the most critical parameters, for the simple reason that it is important to have as many atoms as possible coupled to the nanophotonic device, within its small mode volume.

The temperature of the atom cloud in the MOT chamber following polarization-gradient cooling drops to below 10 μK. Of these 10^9 atoms, about 10% are loaded onto a one-dimensional lattice

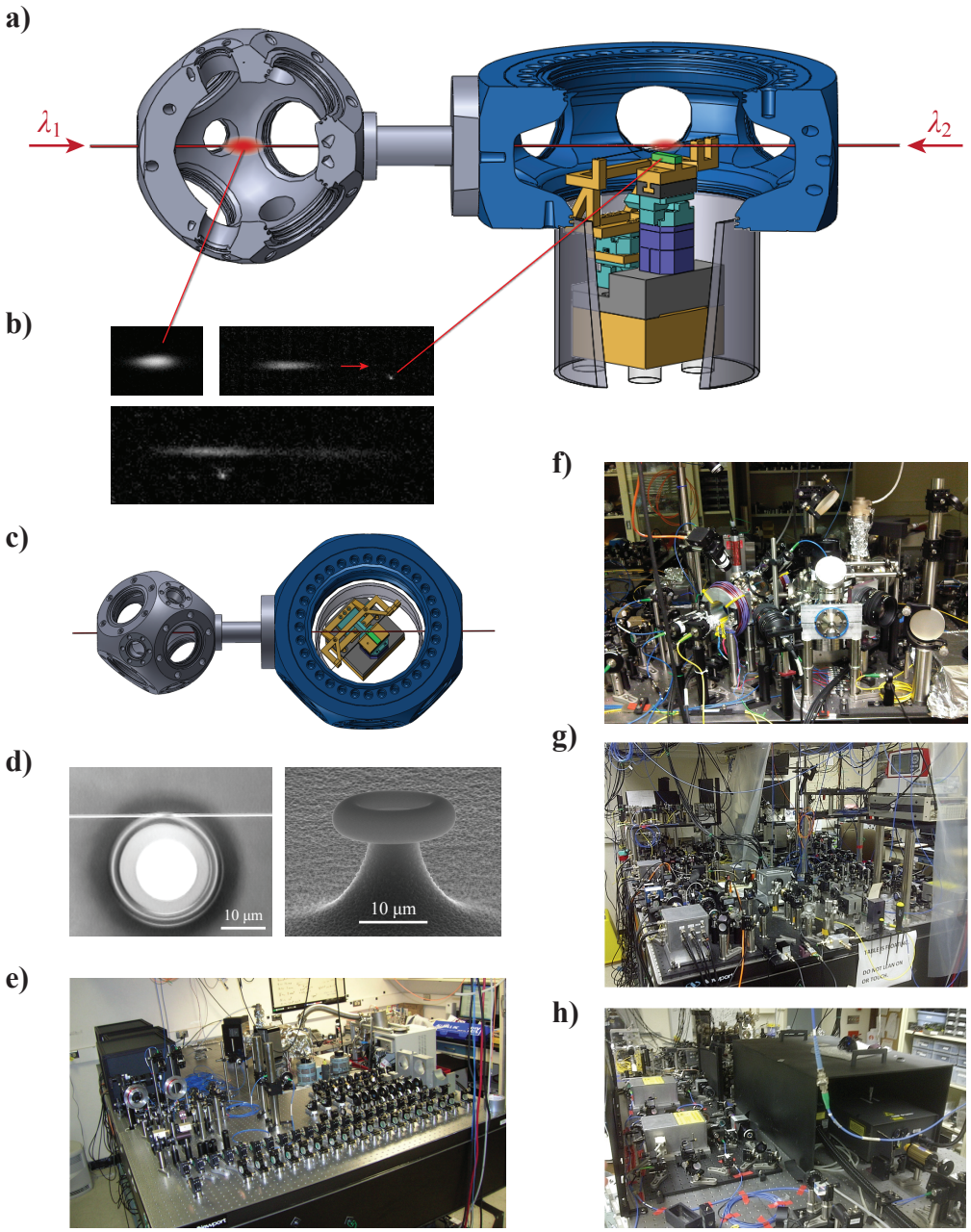

Figure 3.4: **Microtoroid cavity QED experiment setup. a)** Schematic showing two ultra-high-vacuum chambers connected by a differential vacuum tube, where a magneto-optically trapped atom cloud is formed in the source chamber (left), loaded into an optical conveyor belt dipole trap formed by counter-propagating red-detuned beams λ_1, λ_2 whose relative frequency is chirped, transporting the atom cloud to the science chamber where a microtoroid and nanofiber is located, mounted on top of nanopositioners. **b)** CCD camera images of atom cloud fluorescence, showing source atom cloud (top left), cloud being transported to the toroid chip visible as a bright point (top right) and final position at ~ 800 μm above the toroid chip (bottom panel). **c)** Top view. **d)** SEM images of a microtoroid and tapered fiber. **e)** Fresh (blank) optical table in 2007, showing parts to be used to build the setup from scratch. **f-h)** Completed setup where the experiments [10] and [5] were conducted, showing the main two-chamber setup in (f), various external cavity diode lasers, optical devices and optics supporting the experiment in (g), and Ti:Sapph laser (for optical conveyor belt) and home-built tapered amplifier units, with toroid characterization setup in the background (h).

optical dipole trap formed by a pair of counter-propagating red-detuned (with $\lambda_{\rm dip} = 852.43$ nm, 0.08 nm red-detuned from cesium D2 line at 852.35 nm) beams, each with a power of ≈ 170 mW. Now taking into account both D1 and D2 transitions, the effective detuning, Δ, is given by [3]:

$$\frac{1}{\Delta} = \frac{1}{3}\left(\frac{1}{\Delta_1} + \frac{2}{\Delta_2}\right), \tag{3.21}$$

where Δ_i is the detuning from the D_i-line. For the above parameters, $\Delta = -2\pi \times 51.3GHz$. The maximum trap depth U_0 (located at the focus and anti-node of the standing wave) for a pair of counter-propagating linearly polarized Gaussian beams with beam waist size w_0 (Rayleigh length $z_0 = \pi w_0^2/\lambda_{\rm dip}$ and beam radius profile $w^2(z) = w_0^2(1 + z^2/z_0^2)$) is given by

$$U_0 = \frac{\hbar\gamma_0}{2}\frac{P}{\pi w_0^2 I_{\rm sat}}\frac{\gamma_0}{\Delta}, \tag{3.22}$$

where $\gamma_0 = 2\pi \times 5.2$ MHz is the natural linewidth of Cesium D2-line in free-space, $I_{\rm sat} = 1.1$ mW/cm^2 is the corresponding saturation intensity, and P is the total power of both laser beams. In our experiment, the beam's waist size is $w_0 = 300$ μm, constrained by the dimensions of our MOT chamber and science chamber composite setup (note that the FORT beams are launched by beam-launchers located at both ends, from the outside of the composite chamber). Substituting the numbers, we get a maximum trap depth of $U_0 = 1.37$ mK. An atom of mass m trapped in this standing-wave potential oscillates (in harmonic approximation) with frequencies:

$$\Omega_z = 2\pi\sqrt{\frac{2U_0}{m\lambda^2}}, \qquad \Omega_r = \sqrt{\frac{4U_0}{mw_0^2}}, \tag{3.23}$$

where $\Omega_z/2\pi = 971$ kHz and $\Omega_r/2\pi = 3.9$ kHz are the trap frequencies along the axial and radial directions, respectively. Another important parameter to consider in our standing-wave dipole trap is the scattering rate that heats up the atoms, which is given by:

$$R_{\rm sc} = \frac{U_0\gamma_0}{\hbar\Delta}, \tag{3.24}$$

which has the value $R_{\rm sc}/2\pi = 29$ kHz. Each photon scattered adds on average one recoil energy $E_{\rm r} = (\hbar k)^2/2m = 99.1$ nK, so that the heating rate due to photon scattering is given by (the energy E of an atom in the dipole trap potential increases as) $\langle\dot{E}\rangle = 2R_{\rm sc}E_{\rm r} = 35.6$ mK/s. Considering only this effect corresponds to an increase in energy of 1.75 mK over a duration of 50 ms. The measured $1/e$ lifetime of the atom numbers in the standing-wave stationary dipole trap lattice is 50

ms. For more detailed discussions on dipole traps including the loading process, see [3, 95, 141].

We note that in the above case, we have substituted the intensity profile for a standing-wave Gaussian beam forming the one-dimensional lattice as described in detail in [3]. We note that more generally, the dipole trap potential (shift in the ground state energy of the atom due to interaction between the laser electric field and the atom's electric dipole moment due to its atomic polarizability), for the case of large detuning forming a FORT (far off-resonant trap), is given (in rotating-wave approximation) by [95]:

$$U_{\rm dip} = \frac{3\pi c^2}{2\omega_0^3}\frac{\gamma_0}{\Delta} I(\vec{r}), \tag{3.25}$$

where ω_0 is the atom's resonant frequency, γ_0 is the free-space spontaneous decay rate, Δ is the effective detuning given by Eq. (3.21), and $I(\vec{r})$ is the spatial intensity profile at the location of the atom $\vec{r}$. The scattering rate is given by

$$R_{\rm sc} = \frac{\gamma_0}{\hbar\Delta} U_{\rm dip}. \tag{3.26}$$

We note that while the trap potential $U_{\rm dip} \sim I(\vec{r})/\Delta$, the scattering rate $R_{\rm sc} \sim I(\vec{r})/\Delta^2$, so that for a given trap depth $U_{\rm dip}$ it is preferable to have larger intensity $I(\vec{r})$ and detuning Δ. In our case, we are limited by the maximum power that is available, which is $\approx$ 170 mW per beam. We also note that for an arbitrary dipole potential $U = U(\vec{r})$, the trap frequency along a particular direction, say x, is given by applying the harmonic approximation $U_{\rm HO} = m\omega_x^2 x^2/2$ at the location near the trap minimum, such that the trap frequency along x is given by $\omega_x = \sqrt{(2/m)\partial^2 U/\partial x^2}$.

Getting back to our cold atom cloud in the MOT chamber as illustrated in Fig. 3.4 a), we then chirp the relative frequencies between the two counter-propagating FORT beams to move the 10^8 atoms that are loaded into the standing-wave lattice, over a period of $\approx$ 80 ms, to transport the cold atoms into the science chamber 20 cm away, to be released $\approx$ 800 μm above a microtoroid. The conveyor belt motion can be thought of as a stationary standing-wave in a frame moving at a constant velocity given by $v = \lambda\Delta\nu/2$, where $\Delta\nu$ is the relative frequency detuning between the two counter-propagating beams [140]. The direction of the conveyor belt velocity is determined by the sign of the detuning $\Delta\nu$. In the case of our experiment, λ = 852.43 nm, $\Delta\nu$ = 6.35 MHz, giving v = 2.71 m/s. This is approximately equal to simply dividing the distance between the two centers of chambers as illustrated in Fig. 3.4 a), 20 cm, by the total time of $\approx$ 80 ms, v = 20 cm/80 ms = 2.5 m/s. We note that this is also in agreement with the atom cloud fluorescence imaging measurement, with the camera imaging system calibrated directly using an independent ruler. We also note that

one very important and crucial element in the conveyor belt system is to use a smooth conveyor belt acceleration profile from the initial stationary position, in transition to constant velocity state, and in decelerating to the final stop. This qualitative smoothness condition is much more important and critical than the precise values used in the conveyor belt sequences. In our experiment, we optimize the numbers empirically to give our required transport efficiency and distance. We follow the techniques used in [140, 213, 217]. As our final goal is to have single atoms coupled to our microtoroidal resonators, the conveyor belt efficiency and heating rate are not critical for us. After the 80 ms conveyor belt transports over 20 cm, we lose about 90% of our atoms, leaving $\approx 10^7$ atoms at a temperature of 100 μK positioned 800 μm above a microtoroid. The release of these 10^7 atoms then leads to ≈ 10 atoms that have trajectories with locations that lead to strong coupling to the microtoroid's whispering gallery mode via its evanescent field, which are detected in our experiment in real-time. We note that the science chamber is kept to a pressure below 10^{-9} torr by ion pumps.

3.1.2.2 Optics and electronics

In this section, we give a broad overview of the techniques and components used to control and perform detection in the microtoroid experiments described in Chapters 4 and 5. A schematic of the experimental setup and more discussions can be found in Sec. 5.9.

Our laser sources for the microtoroid experiments consist of home-built Littrow design external cavity diode lasers mainly at 852 nm wavelength, locked to cesium D2 transitions (F=4 $\rightarrow$ F'=5 for MOT beams, F=4 $\rightarrow$ F'=3 for repumping beams) via saturated absorption spectroscopy [189], a commercial Newport Vortex Littman-Metcalf design external cavity diode laser tunable by more than 50 GHz, and a frequency-offset locked home-built diode laser (which consists of a reference laser interfered with the output of a frequency-offset laser, whose beatnote is detected by a fast photodetector to generate an error signal in frequency, which is converted to voltage by frequency-to-voltage converter electronic chip, and used to PID-lock the frequency-offset laser through piezoelectric actuation of the grating of the frequency-offset laser), and a Coherent MBR Ti:Sapph laser pumped by 532nm Verdi V-10 and later replaced by Verdi G-10, used to form our standing-wave/conveyor belt FORT. In addition, we use commercial (Toptica) and home-built (based on JILA design in Prof. Jun Ye's group) optical tapered amplifiers, with tapered amplifier chips from M2K and Eagleyard. These laser sources and tapered amplifiers are shown in Fig. 3.4 g-h). Other optical components used but not visible in Fig. 3.4 g) are various optical modulators EOMs (e.g. from New Focus), AOMs (e.g., from Brimrose, or from Inraaction where we could get diffraction efficiencies of $> 95\%$

at 852 nm), MEMS, in-fiber EO/AO/Mach-Zehnder switch (from EOSpace, with switching speed of $\approx$ 10 ns).

The sequences (e.g., MOT loading, cooling, transport, etc.) in the experiment are controlled by LabView programs that we wrote, which communicate with various National Instruments data acquisition cards (e.g., NI PCI-6259, NI PCI-6602 cards) and National Instrument field programmable gate arrays (FPGA) operating at 40 MHz, controlling various home-built and commercial electronic circuits (e.g., from MiniCircuits). An example of the sequences involved in the experiment described in Chapter 5 is: 1 second MOT loading, followed by 25 ms compressed-MOT (CMOT), 5 ms polarization-gradient (PG) cooling, 10 ms loading time into FORT lattice, 0.5 ms conveyor belt acceleration, 82 ms constant velocity time, 0.5 ms deceleration time, and 0.8 ms of waiting time before release of atom cloud. We note that these involve various on/off optical laser switching using AOMs, and frequency and power tuning using analog controls via voltage-controlled-oscillators (VCOs) and voltage-controlled-attenuators (VCAs) that control the RF drivers for AOMs. During this sequence, the toroid is temperature stabilized to maintain its resonant frequency to coincide with cesium D2 line (F=4 $\rightarrow$ F'=5 transition), by using an actively locked Peltier for slow and large temperature range control with error signal generated from a thermistor mounted inside the UHV chamber near the toroid, and by using a heating laser focused on the toroid chip, relatively far from the operating toroid to avoid photons leaking into the probe tapered fiber, for fast temperature control. Here, the error signal is generated by continuously alternating between the frequency-sweeping probe beam and the detection beam. The frequency-sweeping probe beam is split into two beams, one passing through the toroid system locating the toroid's resonance, and another performing saturated absorption spectroscopy. The error signal is then computed from this using LabView, with an overall locking bandwidth of around 8 Hz, which is sufficient for the experiment. Following this frequency-sweeping beam, the toroid is probed with a 'detection beam' set to be resonant to cesium atoms, used to perform real-time detection of single cesium atoms in less than 500 ns. If a cesium atom is detected, the probe beam is switched to the 'probe beam' laser, which may have various frequencies and intensities used to make temporal or spectral measurements.

As discussed in Sec. 5.9, the input and output of the toroid-coupled tapered optical fiber is connected to an array of 99/1 beam-splitters for power attenuation at the input, and 50/50 beam-splitters to perform correlation/coincident measurements of the transmitted and reflected fields. The photons (at a power of $<$ 1 pW) are detected by single photon counting modules (SPCMs) from Perkin-Elmer, which are connected to electronics for processing and acquired by fast acquisition

card P7888 model from FAST ComTec, with 2 ns time-resolution. Brighter beam detections are done using various photodetectors from Thorlabs and from Newport for higher performance (higher bandwidth and lower noise) detections, and we also used various femto-watt photodetectors, e.g., low bandwidth femto-watt photodetectors from New Focus. For imaging, we used various SLR-camera-type composite lenses, preferably with adjustable zooms, as shown in Fig. 3.4 f), giving $\approx 0.1 - 0.2$ numerical aperture, which is sufficient for our purposes mainly for fluorescence imaging of atom clouds and as a microscope (with 10x to 20x zoom) for the toroid to aid toroid-taper spatial alignment. The images are detected by standard CCD cameras (e.g., Sony XCE130 CCD with Sony DC-700 controller), connected to National Instruments image acquisition cards (e.g., NI PCI-1410) and are controllable by LabView. The spatial scale for the cameras can be calibrated directly by using a physical ruler, or by dropping a cloud of atoms and using gravitational acceleration rate as the reference. We note that in the latter, one assumption is that the atom cloud falls at the rate of $g = 9.81$ m/s^2, which may not always be the case, for example if there is residual near-resonant light (when AOMs for the MOT beams are switched 'off') providing deceleration against gravity.

3.1.2.3 Optical/photonic devices and mechanics

As discussed previously, in the microtoroid cavity QED experiments, two optical/photonic devices are central in the experiments, namely the microtoroid silica cavity and the tapered optical fiber used to couple light in and out of the cavity. The fabrication of the microtoroid cavity involves creation of silica microdisks that are then heat-reflowed by a CO_2 laser to become a smooth microtoroid, giving quality factors in excess of 10^9. For our experiments with relatively small dimensions, the cavity quality factors reach above 10^7. Our microtoroid cavities are fabricated by our collaborators Dr. Eric Ostby and Dr. Hansuek Lee, members of the Prof. Kerry Vahala group at Caltech. For more information regarding the fabrication of a microtoroid cavity, see for example [240]. The tapered fibers for our experiments are home-built, as discussed in Sec. 3.2.

We now discuss the integration and positioning of the microtoroid and tapered fiber. As shown in Fig. 3.4 a), the microtoroid chip is positioned on top of a Peltier (shown as green box), on a copper plate in contact with a thermistor. The toroid chip is attached to the copper plate by a vacuum-compatible, conductive double-sided carbon adhesive pad (such as the ones used in SEM sample holders, e.g., from Ted Pella). The copper plate is attached to the Peltier by a UHV-compatible ceramic compound (Cerama Bond 835-M from Aremco Products). The Peltier is then mounted on machined aluminium adapters that mount into a stack of nano-positioners (Attocubes model

100 series). Together with the mounting stack for the tapered fiber (see Fig. 3.4 a)), we have four Attocube positioners, giving x, y, z-linear tunability and one tilt tunability to adjust the axis of the fiber relative to the plane of the toroid cavity. Characterization and calibration of the Attocube positioners is given in Appendix A. We note that despite the nice capabilities of long-range and at the same time nanometer precision positioning by the Attocubes, they need very careful handling and more importantly, they have mechanical resonances at the $\approx$ 200-500 Hz range (at least for these model 100 series) as shown in Appendix A. This leads to amplification of mechanical vibrations from the environment, which leads to instability in the relative position between the toroid and tapered fiber, which then could lead to fluctuations in the optical transmission out of the tapered fiber when the system is positioned at (near) critical coupling condition. In other words, instead of the ideal case where transmission is zero at critical coupling (all things being ideal), the vibrations limit the minimum value of transmission (T) that can be achieved. Indeed, out of all instabilities in our experiment, this mechanical vibration is the limiting factor for the minimum value of T at critical coupling.

One way to overcome this is to actively stabilize the toroid-taper separation distance. This however requires both frequency stabilization as well as position stabilization. With Dr. Elizabeth Wilcut Connolly, we tested this in a separate characterization setup outside our chamber, using Pound-Drever-Hall locking [28] that locks the laser frequency to the toroid cavity resonance; and then while this was operating, we implemented dither locking, where the relative position error signal is obtained by oscillating (dithering) the position at high frequency using the Attocube controller. Although it is quite complex and is not ideal to implement during the experiment, where the complexity is undesirable, in the test we were able to suppress the vibration noise in the low frequency region below 4 Hz by more than 40 dB. More information can be found in [51].

In our experiments, we rely on passive mechanical stability to ensure good floating of our optical table, which is very crucial, and then we place the entire stack of positioners and mount them on top of four little (1 cm diameter $\times$ 1 cm height cylinders) soft silicone rubbers as shown in Fig. 3.4 a). Together, these lead to a stability in transmission of $\delta T < 1\%$ at critical coupling, a significant improvement to the case without the two passive stabilization implementations of $\delta T \approx 10\%$. The soft vibration isolation material is a room-temperature vulcanizing silicone rubber RTV-615 (from GE silicones) that is vacuum-compatible [1]. With these passive stabilizations implemented, we can maintain our transmission to be below $T < 1\%$ at critical coupling in our experiment. We note that looking at the 'noise' that makes up this 1% critical-coupling level, there is a major component

oscillating at a frequency of ≈ 250 Hz, showing that it is due to the mechanical vibrations amplified by the Attocube mechanical resonances. We also note that other sources of noise including the dark-noise of our detectors are significantly below this $T = 1\%$ level.

3.2 Nanophotonic optical fiber as a quantum optics platform

3.2.1 Model

A schematic of a tapered optical nanofiber is shown in Fig. 3.5 a) with its features highlighted. Starting from a standard optical fiber (diameter values given here for a specific fiber example) with jacket diameter $D_{\mathrm{J}} = 400$ μm, buffer diameter $D_{\mathrm{B}} = 250$ μm, cladding diameter $D_{\mathrm{Cl}} = 125$ μm, and core diameter $D_{\mathrm{Cr}} = 5$ μm, a nanofiber is fabricated by pulling the two ends of the single-mode fiber with a heat source positioned at the center. For the fibers fabricated for the experiment described in Chapter 7, the total tapering length is $L_{\mathrm{T}} \approx 7$ cm, and the uniform waist size fiber length is $L_{\mathrm{f}} = 6$ mm. The fiber radius decays exponentially in the transition regions, from the cladding size of $r_{\mathrm{Cl}} = 62.5$ μm down to the nanofiber radius $D_{\mathrm{f}}/2 = a = 215$ nm, as shown in the schematic in Fig. 3.5 a) and experimental datapoints from SEM measurements, in Fig. 3.5 d) and theoretical predictions shown as solid curves in Fig. 3.5 d) in parts (i) and (ii). The Cartesian coordinate systems used are shown in Fig. 3.5 a) with $\{x, y, z\}$ and in cylindrical coordinate $\{r, \phi, z\}$. We note that as the fiber radius decreases from 62.5 μm down to 215 nm, at some stage the fiber core material vanishes and the entire nanofiber is made up only of the cladding material. Here, we no longer have core-cladding guided mode but rather cladding-air guided mode. If the nanofiber radius is sufficiently small, as the case in our experiment, relative to the propagating light wavelength λ, then the nanofiber only supports a single mode, the fundamental mode.

Now consider an input light beam of wavelength $\lambda = 852$ nm, polarized along the x-axis, as shown by the 3D gray arrow illustrating light injected into the nanofiber from the bottom left of Fig. 3.5 a). The fundamental mode supported by the nanofiber of radius $a = 215$ nm is shown in Fig. 3.5 c), where in part (i), the (normalized) absolute value of the electric field $|E|/|E|^{\max}$ taking into account all (c-valued) components E_x, E_y, E_z is shown as a contour plot, with white arrows (vectors) showing the directions of local (real-valued) electric field polarizations $(E_x, E_y)/\sqrt{E_x^2 + E_y^2}$ (note the length of the arrow vectors is normalized). By real-valued, we refer to the plane at optical phase $\theta = 0$, the phase where the beam's polarization field E_x is maximum and $E_z = 0$. At $\theta = \pi/2$, $E_x = E_y = 0$ and E_z is maximum. We note that because of the subwavelength

confinement of the light beam (electromagnetic field), although at the beginning of the tapered fiber (when the radius is still 62.5 μm) we inject a laser beam polarized along x, with negligible E_y and E_z, the polarization structure becomes more complicated at the nanofiber region, as shown in Fig. 3.5 c) for E_x, E_y, E_z. The field has electric field components in all axes x, y, z, and moreover the longitudinal field component E_z is $\pi/2$ phase-shifted relative to the other components. At this small sub-wavelength light confinement regime, these field components can have amplitudes comparable to each other (see Fig. 3.5 c) caption). We also note the field spatial azimuthal symmetry breaking that occurs in this regime.

Despite the complex polarization structure discussed above, which is undesirable, the tapered optical nanofiber platform provides a mean to confine single atoms three-dimensionally, along a one-dimensional array in close proximity $\sim$ 100 nm to the nanofiber surface. One scheme that utilizes two pairs of red-detuned (λ = 937 nm) and blue-detuned (λ = 687 nm) trapping beams polarized along the x-axis (shown in Fig. 3.5 a)) is discussed in Chapter 7. For illustration, we show in this overview in Fig. 3.5 b), a trap potential profile that can be generated under such scheme, that provides three-dimensional confinement along the standing wave lattice with a trap depth of $\approx$ 200 μK, at a distance of $\approx$ 200 nm from the nanofiber surface. Intuitively, the trap is generated by combining a short-range (short λ) blue-detuned repulsive dipole potential and long-range (long λ) red-detuned attractive dipole potential forming a radial potential well (confinement), azimuthal confinement due to the azimuthal symmetry breaking of the mode profile relative to the polarization direction of the guided beam, and axial confinement due to the counter-propagating standing-wave red-detuned beams that form the one-dimensional lattice. We note that the counter-propagating blue-detuned beam is used not for the purpose of generating a trap potential, but to allow minimal intrusion to the internal state of the trapped atoms that will otherwise be significant due to the complex guided mode polarization structure that leads to local elliptical field polarizations that act as pseudo magnetic fields. The trapping scheme is discussed in Chapter 7, along with our experiment that realizes such atom trap, leading to trapping of $\approx$ 200 atoms at 215 nm from the fiber surface.

One of the key enabling capabilities required to realize a nanofiber atom trap as discussed above is the fabrication of a tapered optical fiber with strict specifications especially in relation to its transmission efficiency (single-mode operation), precise and repeatable nanofiber shape profile and dimensions, and the ability for the nanofiber to carry relatively large amount of power inside a UHV vacuum environment. We discuss our fabrication techniques and results in Chapter 7. Figure 3.5 d) shows the results of seven fabricated nanofiber samples as measured by SEM. Most of these fibers

have efficiencies $> 97\%$, with measured shape profile (especially the nanofiber waist radius) in agreement with the theoretical predictions by $< 5\%$ error, and we have tested the ability of these nanofibers to carry laser beams with optical power exceeding 200 mW inside a vacuum environment. The realization of this nanofiber device with these strict requirements and good yield/repeatability is not a trivial task; it involved many months of optimization and improvements, as will be discussed in Chapter 7.

3.2.1.1 Fundamental nanofiber mode

When the radius a of an optical fiber is reduced well below the propagating field wavelength λ, the resulting cladding-to-air waveguide supports only the "hybrid" fundamental mode HE_{11} [129, 237]. In this strongly guiding regime, a significant fraction of energy of the HE_{11} mode is carried in the form of an evanescent wave outside of the nanofiber. The evanescent field intensity is azimuthally asymmetric when the input polarization is linear [129, 237]. Fig. 3.5 c) i) shows the electric field intensity $|E|^2 = |E_x|^2 + |E_y|^2 + |E_z|^2$ in a plane transverse to the fiber for a single, linearly-polarized beam. The unit vectors $(\mathbf{e}_x, \mathbf{e}_y, \mathbf{e}_z)$ shown in Fig. 3.5 a) form the basis of the (x,y,z) frame, and (r, ϕ) are the cylindrical coordinates in the transverse plane (x,y).

The fundamental mode HE_{11} is often referred to as "quasi-linear" when excited with a linearly polarized input beam. However, for a dielectric waveguide in the strong-guiding regime with indices of refraction $n_1 \approx 1.5$ inside the waveguide and $n_2 \approx 1.0$ outside, the HE_{11} mode actually exhibits a significant ellipticity for $a \lesssim \lambda/2$, leading to vector shifts of the Zeeman sublevels. Formally, for a linearly polarized input, the evanescent field $\mathbf{E} = (E_x, E_y, E_z)$ of the fundamental mode propagating in the fiber can be expressed as follows for $r \geq a$ [129, 237, 205]:

$$
\begin{aligned}
E_x(r,\phi,z,t) &= A_{\text{lin}} \frac{\beta_{11} J_1(h_{11}a)}{2 q_{11} K_1(q_{11}a)} && \text{(3.27a)}\\
&\quad \times [(1-s_{11}) K_0(q_{11}r)\cos(\varphi_0) + (1+s_{11}) K_2(q_{11}r)\cos(2\phi-\varphi_0)] e^{i(\omega t - \beta_{11} z)},\\
E_y(r,\phi,z,t) &= A_{\text{lin}} \frac{\beta_{11} J_1(h_{11}a)}{2 q_{11} K_1(q_{11}a)} && \text{(3.27b)}\\
&\quad \times [(1-s_{11}) K_0(q_{11}r)\sin(\varphi_0) + (1+s_{11}) K_2(q_{11}r)\sin(2\phi-\varphi_0)] e^{i(\omega t - \beta_{11} z)},\\
E_z(r,\phi,z,t) &= i A_{\text{lin}} \frac{J_1(h_{11}a)}{K_1(q_{11}a)} K_1(q_{11}r)\cos(\phi-\varphi_0) e^{i(\omega t - \beta_{11} z)}, && \text{(3.27c)}
\end{aligned}
$$

with

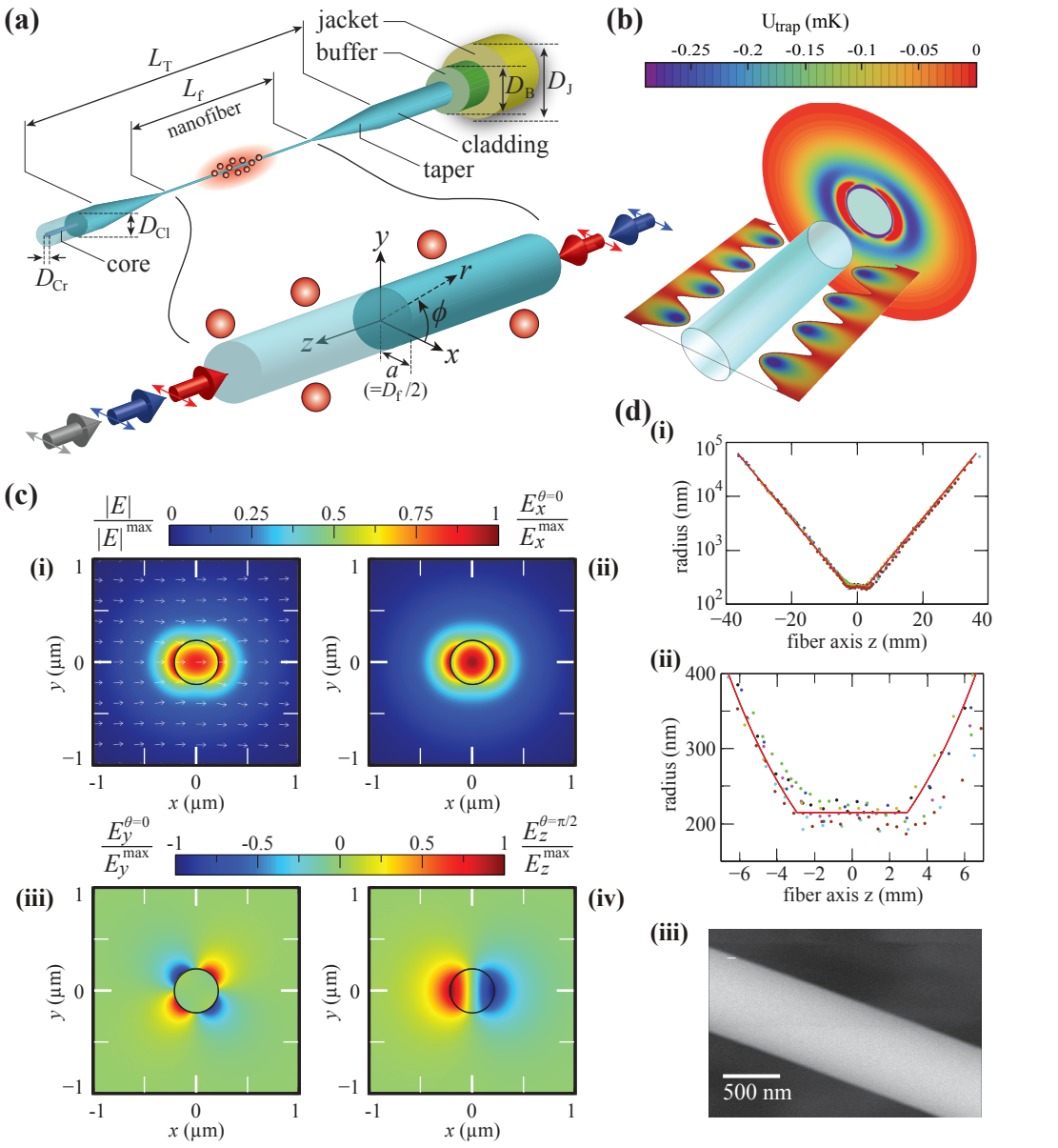

Figure 3.5: **Tapered optical nanofiber. a)** Schematic of a tapered nanofiber, showing fiber jacket (diameter D_J), buffer (diameter D_B), tapering region (total end-to-end length L_T), nanofiber region (L_f) with uniform waist radius $a = D_f/2$, and fiber cladding (diameter D_{Cl}) and core (diameter D_{Cr}). Bottom: Two pair of blue- and red-detuned x-polarized beams form atom trapping potential as shown in b) and x-polarized probe beam shown by the gray arrow. **c)** Normalized electric field $|E|$ profiles and the components $\{E_x^\theta, E_y^\theta, E_z^\theta\}$ (where θ indicates the optical phase and location along the z-axis. E.g., $\theta = 0 \leftrightarrow z = 0, \theta = \pi/2 \leftrightarrow z = \lambda/4$) for the nanofiber fundamental HE_{11} mode polarized along x, with $E_x^{max} = 0.892|E|^{max}, E_y^{max} = 0.224|E|^{max}, E_z^{max} = 0.453|E|^{max}$. **d)** Theoretical prediction and experimental data of tapered fiber radius (r) profile along the fiber axis (z), measured from hundreds of SEM images taken from seven fabricated tapered fiber samples, such as the one shown in (iii).

$$s_{11} = \left[\frac{1}{(h_{11}a)^2}+\frac{1}{(q_{11}a)^2}\right]\left[\frac{J_1'(h_{11}a)}{h_{11}aJ_1(h_{11}a)}+\frac{K_1'(q_{11}a)}{q_{11}aK_1(q_{11}a)}\right], \tag{3.28a}$$

$$h_{11} = \sqrt{k_0^2n_1^2-\beta_{11}^2}, \tag{3.28b}$$

$$q_{11} = \sqrt{\beta_{11}^2-k_0^2n_2^2}. \tag{3.28c}$$

Here, ϕ denotes the azimuthal position in the transverse plane (Fig. 3.1 a), φ_0 indicates the polarization axis for the input polarization relative to the x axis, n_1 and n_2 are the indices of refraction inside and outside the waveguide, β_{11} is the mode propagation constant, $1/h_{11}$ is the characteristic decay length for the guided mode inside the fiber, $1/q_{11}$ is the characteristic decay length for the guided mode outside the fiber, A_{lin} is the real-valued amplitude for the linearly polarized input, J_l is the l-th Bessel function of the first kind, and K_l is the l-th modified Bessel function of the second kind.

The normalization constant A_{lin} is given by:

$$A_{\text{lin}} = \sqrt{2}\left(\frac{4\mu_0\omega P}{\pi a^2\beta_{11}}\right)^{1/2}(D_{\text{in}}+D_{\text{out}})^{-1/2}, \tag{3.29}$$

where

$$\begin{aligned} D_{\text{in}} &= [(1-s_{11})(1+(1-s_{11})\frac{\beta_{11}^2}{h_{11}^2})(J_0^2(h_{11}a)+J_1^2(h_{11}a))+ \\ &\quad +(1+s_{11})(1+(1+s_{11})\frac{\beta_{11}^2}{h_{11}^2})(J_2^2(h_{11}a)-J_1(h_{11}a)J_3(h_{11}a))], \end{aligned} \tag{3.30}$$

$$\begin{aligned} D_{\text{out}} &= \frac{J_1^2(h_{11}a)}{K_1^2(q_{11}a)}[(1-s_{11})(1-(1-s_{11})\frac{\beta_{11}^2}{q_{11}^2})(K_0^2(q_{11}a)-K_1^2(q_{11}a))+ \\ &\quad +(1+s_{11})(1-(1+s_{11})\frac{\beta_{11}^2}{q_{11}^2})(K_2^2(q_{11}a)-K_1(q_{11}a)K_3(q_{11}a))]. \end{aligned} \tag{3.31}$$

Here $D_{\text{in}}/(D_{\text{in}}+D_{\text{out}})$ and $D_{\text{out}}/(D_{\text{in}}+D_{\text{out}})$ are the fractions of the power of the fields that propagate inside and outside of the nanofiber, $\omega = 2\pi c/\lambda$ with the free-space wavelength λ, and P is total propagating power given by

$$P = \int_0^{2\pi} d\phi \int_0^a \langle S_z\rangle r dr, \tag{3.32}$$

where $\langle S_z\rangle$ is the z-component of the cycle-averaged Poynting vector $\langle\vec{S}\rangle = \frac{1}{2}\text{Re}\left[\vec{E}\times\vec{H}^*\right]$, which quantifies the energy flux of the electromagnetic field in the propagation direction along the nanofiber

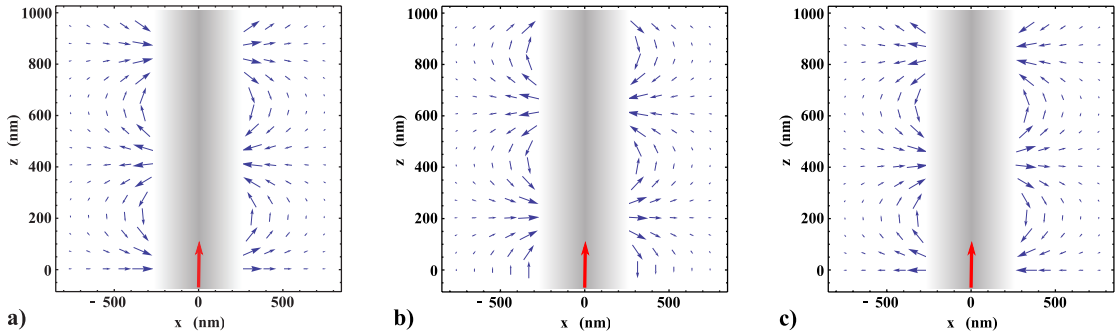

Figure 3.6: **Electric field**, $\mathbf{E}(x, y, z, t)$ of a single propagating beam in the plane $y = 0$. The input beam is x-polarized. The electric field $\mathrm{Re}[\mathbf{E}(x, y, z, t)]$, with $\mathbf{E}(x, y, z, t)$ defined as in Eq. 3.27, is shown by the blue arrows. The red arrow indicates the beam propagation direction. The field is shown for **a)** $\omega t = 0$, **b)** $\omega t = \pi/2$, and **c)** $\omega t = \pi$.

axis. Note that in the ideal case where the tapered nanofiber transmission efficiency is 100%, the total propagating power P is equal to the optical power measured directly at the output of the tapered optical fiber, which also equal to the power of the injected beam (assuming 100% input coupling efficiency). Complete equations for nanofiber fundamental modes for circular and quazi-linear polarizations can be found in [247, 129, 237, 205].

It is clear from Eq. (3.27) that the electric field intensity is not azimuthally symmetric. For a beam polarized along $\mathbf{e}_x$, i.e., $\varphi_0 = 0$, the intensity at the fiber's outer surface is maximum for $\phi = 0,\ \pi$ and minimum for $\phi = \pm\pi/2$.

Notably, the evanescent modes of the nanofiber have a significant longitudinal component E_z along the fiber propagation direction, which is $\pi/2$ out-of-phase with the transverse components (E_x, E_y) (Eq. (3.27c)). At the outer fiber surface, E_z is maximum for $\phi = \varphi_0, \varphi_0 + \pi$ (i.e., along the input polarization axis), and vanishes for $\phi = \varphi_0 \pm \pi/2$. For an x-polarized input at 937 nm and a nanofiber of radius $a = 250$ nm, $\frac{|E_z|^2}{|E|^2}\,(r = a_+, \phi = \varphi_0) \simeq 20\%$. As a consequence, the polarization of a single propagating beam will be elliptical everywhere except for $\phi = \varphi_0 \pm \pi/2$. The ellipticity of the beam will be maximum for $\phi = \varphi_0,\ \varphi_0 + \pi$ as is illustrated in Fig. 3.6, giving rise to significant vector shifts, which we discuss in Section 7.2.

We can re-write Eqs. (3.27) as follows:

$$E_x(r, \phi, z, t) = Ae^{i(\omega t - \beta_{11} z)}, \tag{3.33a}$$

$$E_y(r, \phi, z, t) = Be^{i(\omega t - \beta_{11} z)}, \tag{3.33b}$$

$$E_z(r, \phi, z, t) = iCe^{i(\omega t - \beta_{11} z)}, \tag{3.33c}$$

where A, B, and C are real functions of r and ϕ. In particular, if one combines a forward-propagating beam $\mathbf{E}^{(\mathrm{fwd})}$ expressed as Eq. (3.33) with a backward-propagating beam of same amplitude and input polarization $\mathbf{E}^{(\mathrm{bwd})} = Ae^{i(\omega t+\beta_{11}z)}\mathbf{e}_x + Be^{i(\omega t+\beta_{11}z)}\mathbf{e}_y - iCe^{i(\omega t+\beta_{11}z)}\mathbf{e}_z$, the total field can be expressed as:

$$\mathbf{E}^{(\mathrm{tot})} = \mathbf{E}^{(\mathrm{fwd})} + \mathbf{E}^{(\mathrm{bwd})} = 2\left[A\cos(\beta_{11}z)\mathbf{e}_x + B\cos(\beta_{11}z)\mathbf{e}_y + C\sin(\beta_{11}z)\mathbf{e}_z\right]\cdot e^{i\omega t}. \tag{3.34}$$

The resulting electric field $\mathbf{E}^{(\mathrm{tot})} = \mathbf{E}^{(\mathrm{fwd})} + \mathbf{E}^{(\mathrm{bwd})}$ forms an optical lattice with spatially rotating linear polarization as illustrated in Fig. 3.7. In particular, the polarization state of the field rotates between the pure linear x and z-polarizations along z at $\phi = 0$, as illustrated in Fig. 3.8.

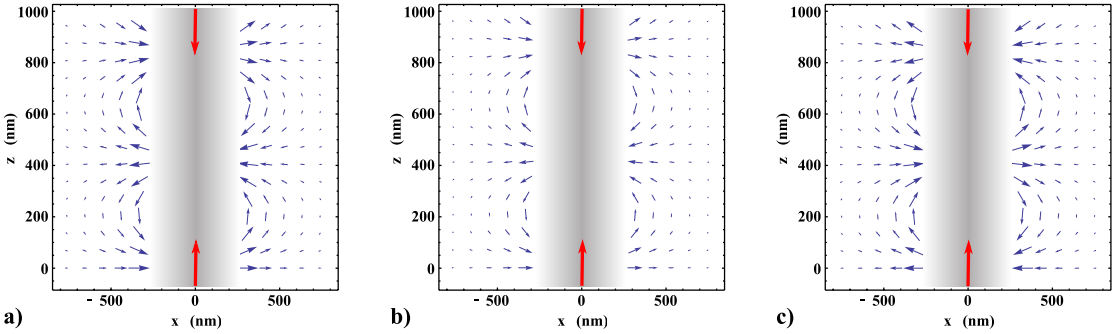

Figure 3.7: **Total electric field**, $\mathbf{E}(x, y, z, t)$ for two counter-propagating beams in the plane $y = 0$. The input beams are x-polarized. The electric field $\mathrm{Re}[\mathbf{E}(x, y, z, t)]$ is shown by the blue arrows. The red arrows indicate the beams' propagation directions. The electric field is shown for **a)** $\omega t = 0$, **b)** $\omega t = \pi/4$, and **c)** $\omega t = \pi$. As opposed to Fig. 3.6, the polarization of the electric field is linear at any point $|\mathbf{r}| > a$ (i.e., the polarization vector has no ellipticity and $\mathbf{E}$ does not rotate in time at a given position $\mathbf{r}$ as in 3.6).

3.2.1.2 Atom-photon interactions with nanofibers

Figure 3.9 shows calculation results for $\lambda^2/A_{\mathrm{eff}}$ with $\lambda = 852$ nm and $A_{\mathrm{eff}} = P/I(x, y)$ where P is the total propagating power as given by Eq. (3.32), and $I = I(x, y) = \frac{c\epsilon_0}{2}\mathrm{Re}[|E(x, y)|^2]$ is the field intensity as a function of the electric field $E(x, y)$ at position (x, y). Recall as discussed in Sec. 2.5.1 that the quantity $1/A_{\mathrm{eff}}$, as conveniently normalized in units of $1/\lambda^2$, is related to the scattering ratio $R_{\mathrm{sc}} = \sigma/A_{\mathrm{eff}}$ with $\sigma = \frac{3\lambda^2}{2\pi}$ the absorption scattering cross-section of the atom in free-space. Note however that this simple formula is only valid in cases such as a weakly focused light interacting with an atom. For cases involving strongly focused light, or in our case sub-wavelength nanophotonic waveguides, the scattering rate, which is related to the amount of absorption by an atom is more complicated than the above simple formula, as discussed in Sec. 2.5.1. Nonetheless,

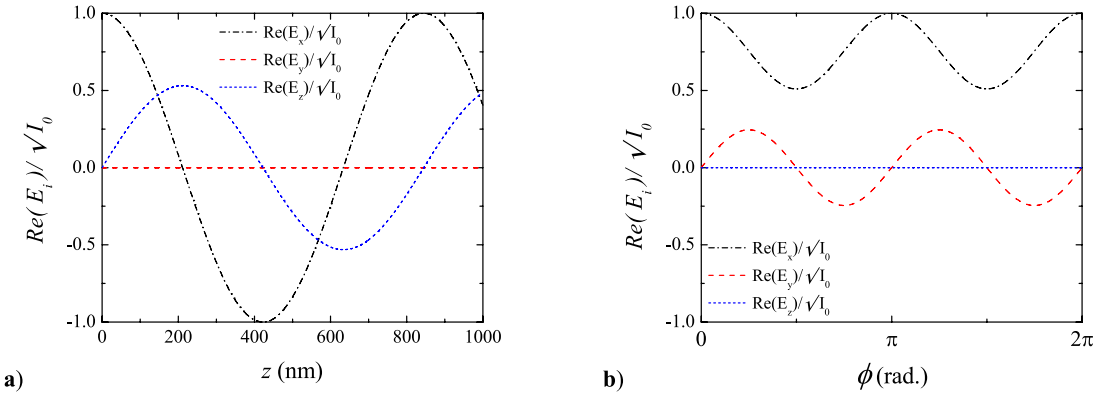

Figure 3.8: **Electric field amplitude after interference**, $\mathbf{E}^{(\mathrm{tot})} = \mathbf{E}^{(\mathrm{fwd})} + \mathbf{E}^{(\mathrm{bwd})}$ of two $\lambda = 937$ nm beams (x-polarized inputs with $\varphi_0 = 0$) with $\delta_{fb} = 0$, at $t = 0$ and $r = a_+$. The fields are normalized to the intensity I_0 at $r = a_+$, $\phi = 0$, $z = 0$. **a)** Axial direction z (at $\phi = 0$). **b)** Azimuthal direction ϕ (at $z = 0$). In particular, $\mathbf{E}^{(\mathrm{tot})}$ has a fixed linear polarization at any given point $\mathbf{r}$ which rotates as $\mathbf{r}$ is varied.

the scattering ratio (which can be interpreted as the strength of atom-photon interaction) is still proportional to $1/A_{\mathrm{eff}}$ within the discussion of Sec. 2.5.1. It is therefore informative to look at the distribution of $\lambda^2/A_{\mathrm{eff}}$ as a function of space.

For a nanofiber with radius $a = 215$ nm (the radius of our fiber used in the experiment described in Chapter 7), the distributions of $\lambda^2/A_{\mathrm{eff}}$ for quasi-linear and circular polarization probe beams are shown in Fig. 3.9 a) and b) respectively. On the right hand side of the contour plots are the corresponding cross-sections at $y = 0$ and $x = 0$, for varying nanofiber radius a. The curves colored in red, blue, green, magenta refer to nanofiber radii of $a = 196$, 215, 250, 150 nm. The radius of 196 nm is obtained from $a = a_{\mathrm{opt}} = 0.23\lambda$, the 'optimum' nanofiber radius that leads to maximum $\lambda^2/A_{\mathrm{eff}}$ at the surface of the fiber $r = a = a_{\mathrm{opt}}$, which holds universally true for any λ [247]. For the plots in Fig. 3.9, we set $\lambda = 852$ nm. Note that as seen in the figures, the small fiber ($a = 150$ nm) has associated with it a large mode area, which leads to a smaller field intensity near the fiber (hence the smaller value of $\lambda^2/A_{\mathrm{eff}}$), but it extends over a larger spatial area around the fiber. For smaller diameter, at larger distances in x and in y, the value $\lambda^2/A_{\mathrm{eff}}$ eventually becomes larger compared to the other larger nanofibers. We note that in our fiber trap experiment, the location of the trap minimum is at $x - a = 215$ nm and y=0, corresponding to the value $\lambda^2/A_{\mathrm{eff}} \approx 0.15$.

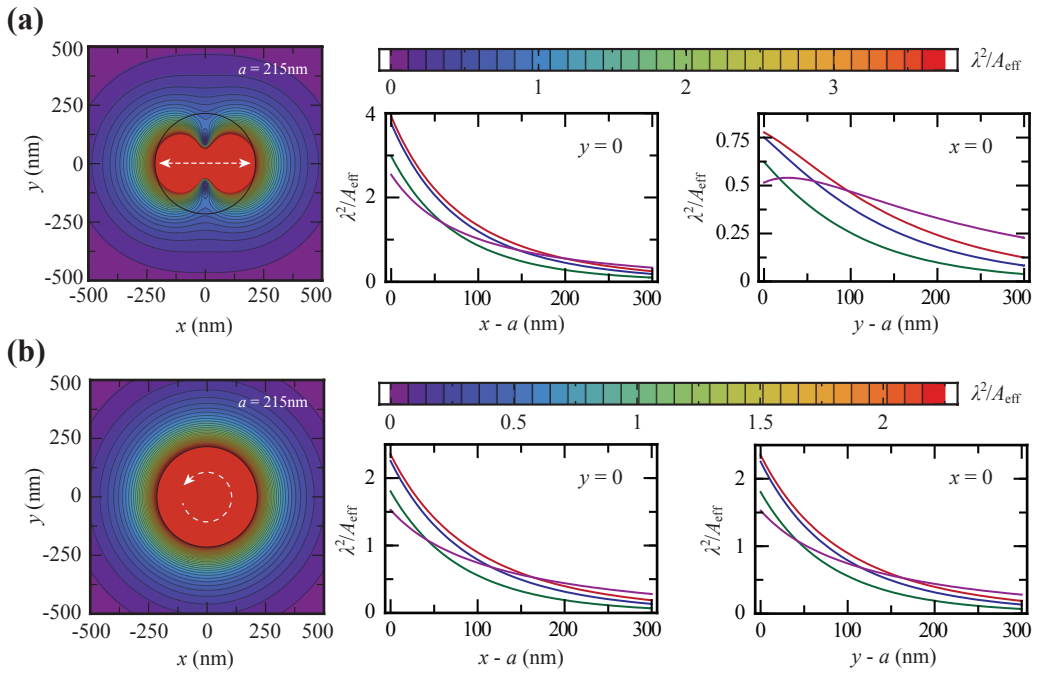

Figure 3.9: **Nanofiber mode effective area.** Contour and cross-sectional plots of λ^2/A_{eff} showing atom-photon interaction strength profile, for a nanofiber HE_{11} mode, x-polarized in (a) and circularly-polarized in (b). The contour plot corresponds to nanofiber radius $a = 215$ nm. For the cross-sectional plots, the curves colored in red, blue, green, magenta correspond to $a = a_{\text{opt}} = 0.23\lambda = 196$ nm (the optimum fiber radius that holds for any λ; here we choose $\lambda = 852$ nm), $a = 215$ nm, $a = 250$ nm, $a = 150$ nm respectively.

3.2.2 Experiment and fabrication setups

The heart of the experimental and fabrication setups for our nanofiber trap experiment described in Chapter 7 is shown in Fig. 3.10, where we utilized the trapping scheme discussed in Sec. 7.2. The realization and achievements made in our experiment using tapered nanofiber platform are a result of collaboration and work of many individuals, which I would like to especially acknowledge here. First and foremost, I would like to acknowledge the group of Prof. Arno Rauschenbeutel of University of Vienna for the pioneering work in optical nanofiber system, which forms the basis of our system. I would like to acknowledge members of our team who worked on the theory, experiment, and nanofiber fabrication aspects for our nanofiber trap experiment: Akihisa Goban, Kyung Soo Choi, Clement Lacroute, Ding Ding, Martin Pototschnig, Tobias Thiele, and Nate Stern. It has been a great priviledge and opportunity to work together with these great individuals who have contributed to the success of our exciting joint experiment. This work was carried out under the guidance and supervision of my advisor, Prof. Jeff Kimble at Caltech.

Fig. 3.10 b) shows a photograph of the actual chamber, with red scattered light visible along the thin nanofiber part of the tapered optical fiber pointed by the white arrow in the figure. The setup consists of a vacuum chamber with large windows, a cesium getter source inside the chamber kept at ultra-high-vacuum by an ion pump, and a piece of nanofiber mounted (by UV glues) on an aluminium 'fork' mount as shown in part a) of the figure. On the outside is a set of quadrupole coils in anti-Helmholtz configuration, magnetic coils to null background magnetic fields, and three pairs of counter-propagating red-detuned beams that together form a magneto-optical trap of a cold atom cloud with diameter $\approx$ 1 mm (with a resonant optical depth of $\approx$ 6) that is polarization-gradient cooled and overlaped with the nanofiber positioned at the center of the MOT cloud. During the dissipative polarization-gradient cooling process (for $\approx$ 10 ms), the cold atoms are loaded into the two-color evanescent trap with a trap depth of $\approx 270\ \mu$K, formed by counter-propagating red-detuned (λ = 937 nm) and blue-detuned (λ = 687 nm) beams with total counter-propagating powers of 2 $\times$ 0.4 mW = 0.8 mW, and 2 $\times$ 5 mW = 10 mW respectively. The traps are located at 215 nm from the fiber surface, with trap frequencies $\{\nu_r, \nu_\phi, \nu_z\} = \{199, 35, 273\}$ kHz. From absorption measurement of probe light that propagates through the tapered fiber, we infer a total of up to $\approx$ 825 trapped atoms (total optical depth of $d_{N=825} = 66$, single atom optical depth $d_1 = 0.08$, where the transmittance $T = e^{-d_N}$ and N is the number of trapped atoms). We infer the single atom optical depth $d_1 = 0.08$ from a saturation measurement with 224 trapped atoms ($d_{N=224} =$ 18).

The probe absorption measurement requires decoupling of the relatively large trapping beam power $P \approx 10$ mW from the probe beam with power $P \approx 0.1$ pW by orders of magnitude. We achieve this by using a pair of volume Bragg gratings (VBGs) at the input side of the fiber to combine the probe beam and the trap beams, and another pair of VBGs at the output side of the fiber to separate the trap beams from the probe beam. Our pair of VBGs provide ~ 180 dB extinction ratio with $> 95\%$ diffraction efficiency. The VBG is a custom holographic grating from OptiGrate, investigated by Dr. Kyung Soo Choi working with Dr. Vadim Smirnov and Dr. Igor Ciapurin at OptiGrate [44].

The setups for taper pulling fabrication are shown in Fig. 3.10 c-d) for our old taper pulling setup and in Fig. 3.10 e-f) for our new taper pulling setup used in nanofiber trap experiments. Here we give an overview of the key differences between the old and new setups; more detailed discussion is given in Chapter 7. There are a couple of key differences between the old and new taper pulling setups; some are visible in the figures. Firstly, our new setup uses much more precise and better-controlled motorized stages, which allow not only precise and repeatable positioning, but also create effective oscillation of the heat source, increasing the heating region, leading to better quality tapers (for ensuring desired tapered fiber shape profile, transmission efficiency, and single-mode condition). Secondly, in the new setup the fabrication process is carried out inside a (specified class 100) clean-hood, which is critical in ensuring a clean nanofiber product, important in ensuring high power-handling capability by the nanofiber inside a vacuum environment. Thirdly, we use a hybrid hydrogen-oxygen torch as a heating source instead of an oxygen-only flame. While it is not clear that this is critical to producing a good quality nanofiber, this provides tunability of the flame temperature for a given flame torch alignment, oxygen flow rate, ambient air and nozzle type. More details are discussed in Chapter 7.

3.3 Nanophotonic waveguide and cavity as a cavity QED platform

In this section we investigate two nanophotonic waveguide structures namely single nanobeam and double nanobeam structures, discussed in the subsequent subsections. While we concentrate mainly on nanophotonic waveguides in this section, we note the potential of forming optical resonators by fabricating a pair of photonic crystal mirrors placed at both ends of the waveguide. Another potential consideration is to form a periodic structure along a nanophotonic waveguide, which will

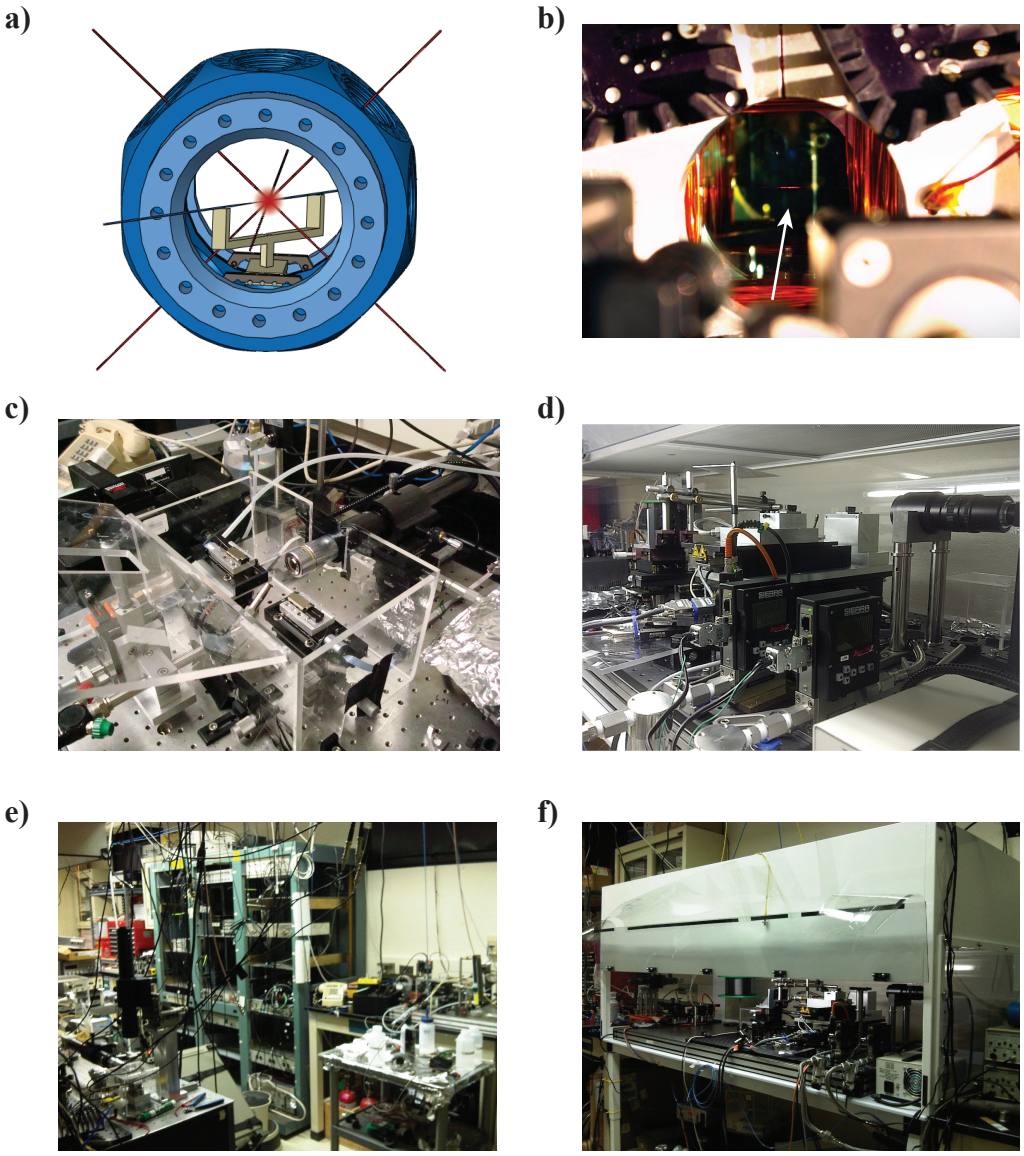

Figure 3.10: **Tapered nanofiber fabrication and experiment overview. a)** Schematic showing a nanofiber mounted on an aluminium holder inside an UHV chamber, with three pairs of counter-propagating magneto-optical trapping and cooling beams forming cold atom cloud overlapped with the nanofiber. **b)** Photograph of the vacuum chamber, with arrow pointing towards the red-glowing nanofiber. **c, e)** Close-up and environment pictures of our old taper-pulling setup. **d, f)** Close-up and clean-hood environment pictures of our improved taper-pulling setup used to fabricate tapered nanofibers for our nanofiber atom trap experiment.

create band-structures that may be exploited to increase atom-photon interaction strength and also other physics based on many-body interactions. These are discussed in Chapter 8.

3.3.1 Single nanobeam

In this section, we describe a nanobeam structure that functions as a nanophotonic device. The general structure discussed in this section has been designed and initially fabricated by the Painter group, with inputs from Su-Peng Yu in our group. A single nanobeam structure consists of four main sections as illustrated in Fig. 3.11 a). Starting from a buffer-stripped standard single-mode bare core-cladding fiber (e.g., with core diameter of 5 μm and cladding diameter of 125 μm), the first section (labeled z1 in the figure) is the butt-coupling section, where the core-cladding silica (refractive index 1.45) optical fiber guided mode is matched to the mode of the nanobeam-air, silicon nitride (refractive index 2) guided mode (e.g., x1 = 150nm, z1 = 10 μm). This section is mechanically supported by a small tether that connects to the chip substrate (z2 = 100 nm). In the second section (z3), the small-sized nanobeam (i.e., large-sized field mode) is adiabatically tapered into larger-sized nanobeam (smaller-sized field mode) to match to the small mode cross-section size of the desired nanophotonic waveguide (x2 varies from 150 nm to 300 nm as $x2^3$ and x3 varies linearly to 1000 nm, z3 = 300 μm, z4 = 10 μm). This part is supported by about 15 tethers over the length z5 = 3.26 μm, followed by a linear decrease in width (x4) from 1000 nm to 300 nm over the length z6 = 10 μm (x5 $\approx$ 75 μm). Next, our third section, which is the main section, is a uniform nanophotonic waveguide with rectangular cross-section of width w = x6 = 300 nm and height h = y1 = 200 nm (the thickness of the silicon nitride substrate). The length of the nanobeam ranges from z7 $\sim 100 - 1000$ μm. Finally in the fourth section is a photonic crystal mirror (x7 varies linearly from 300 nm to 500 nm, z8 = 10 μm) made up of 10 tapered holes followed by 22 mirror holes (lattice constant between holes 340 nm, diameter ϕ1 is tapered from zero to ϕ2 = 200 nm, distributed over z9, z10, z11). Note that the abovementioned parameter values are actual SEM measured values (which are different to the CAD design parameters due to shrinkages and expansions induced in the fabrication process) for a particular successful design by Su-Peng Yu (Kimble group) in collaboration with Painter group [73]. It is described here to give a sense of the geometry of our device. Optimization was conducted by Su-Peng Yu and Sean Meenehan using Lumerical software that maximizes optical quality as the light propagates from the tip of the cleaved fiber, all the way to the photonic crystal mirror, is reflected, and is injected back into the optical fiber, taking into account structural stability. We note that the bare fibers are glued onto the V-grooves, limiting

the minimum distance between neighboring fiber-nanobeam devices to a few 100 μm. As shown in Fig. 3.11 a) and b) i), the chip has a through-hole of size X0 $\approx$ 5 mm by Z0 $\approx$ 2 mm, which allows multiple devices (e.g., five devices) to be fabricated on the whole chip of size X1 = Z1 = 1 cm. SEM images taken for a similar chip are shown in Fig. 3.11 b) showing the overall structure in i), the fiber-to-nanobeam butt-coupling in ii), the nanophotonic waveguide in iii), and the photonic crystal mirror in iv). From Lumerical simulation by Su-Peng Yu of one of the fabricated photonic crystal mirrors, using dimensions measured by the SEM: lattice constant = 340 nm, width = 500 nm, hole diameter = 200 nm, 10 linear taper sites, 15 mirror sites, followed by 10 linear tapering-out sites, the reflectance is R = 99% (T=0.9%) for in-plane (x) polarization and transmittance is T = 97% ($R < 0.1\%$) for normal-to-plane (y) polarization, with the rest of the power is absorbed or lost. We note that these number can be further optimized.The mirror bandwidth is $\pm$ 1 THz, with similar reflectances and transmittances.

In the initial design stage of the nanobeam waveguide structure, my principal contribution has been in the investigation of optical modes of the nanobeam structure, in the context of atom-photon interactions as discussed below. I would like to acknowledge the contributions of Sean Meenehan and Richard Norte from the Painter group, and Su-Peng Yu from our group, on the structure design and optimizations, critical for the fabrication of the device shown in Fig. 3.11 b).

The fundamental nano-waveguide mode for an x-polarized input beam with rectangular cross-section of $w \times h$ = 300 $\times$ 200 nm is shown in Fig. 3.11 c). As discussed in Sec. 3.2, in this sub-wavelength regime of tight electromagnetic field confinement, complex field polarizations arise despite a linearly polarized input beam. As seen in part c) of the figure, it involves all three (E_x, E_y, E_z) components that have comparable amplitudes. Note that the longitudinal component E_z is $\pi/2$ out of phase relative to the E_x and E_y components. The exact ratios of the various field components are given in the figure caption. In part i) of the figure, the (normalized) amplitude of the electric field $|E|/|E|^{\max}$ is shown, taking into account all (c-valued) components E_x, E_y, E_z, with white arrows (vectors) showing the directions of local (real-valued) electric field polarizations $(E_x, E_y)/\sqrt{E_x^2 + E_y^2}$ (note the length of the arrow vectors is normalized). The real parts are at the optical phase $\theta = 0$, and the imaginary parts are $\pi/2$ out of phase at $\theta = \pi/2$.

In the same spirit as in Sec. 3.2.1.2, here we show the calculation result for the distribution of λ^2/A_{eff}, a measure of atom-photon coupling strength of the nanophotonic waveguide, with λ = 852 nm, and $A_{\text{eff}} = A_{\text{eff}}(x, y)$. For discussions on the definition and relevance of this quantity, please refer to Sec. 3.2.1.2 where we discussed the same quantity in nanofiber platform. The result for this

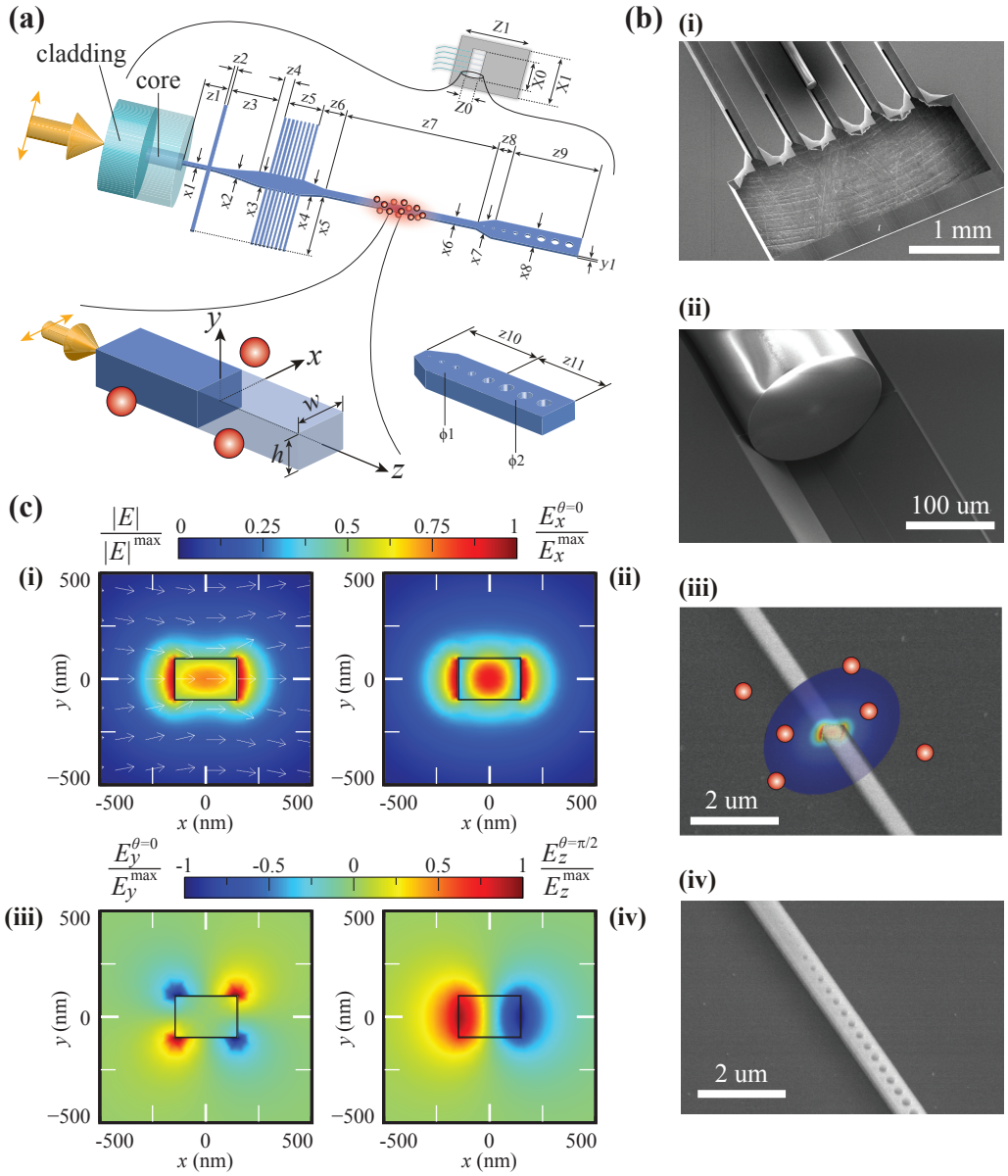

Figure 3.11: **Nanophotonic beam and mirror.** **a)** Schematic of a nanobeam device showing optical fiber to silicon nitride waveguide butt-coupling, adiabatic adapter to nanobeam mode (z1-z6), a nanobeam waveguide with width w and height h, followed by a photonic crystal mirror (z8-z9). The dimensions are discussed in the text. **b)** SEM images of a fabricated device (courtesy of Painter group), showing a sample structure with $\sim$ mm size thru-hole in (i), fiber butt coupling (ii), nanobeam waveguide with electric field profile (iii), and photonic crystal mirror at the end (iv). **c)** Normalized electric field $|E|$ profiles and the components $\{E_x^\theta, E_y^\theta, E_z^\theta\}$ (where θ indicates the optical phase and location along the z-axis). E.g., $\theta = 0 \leftrightarrow z = 0, \theta = \pi/2 \leftrightarrow z = \lambda/4$) for the nanobeam fundamental HE_{11} mode polarized along x, with $E_x^{\max} = 0.840|E|^{\max}, E_y^{\max} = 0.340|E|^{\max}, E_z^{\max} = 0.560|E|^{\max}$.

rectangular nanophotonic waveguide is shown in Fig. 3.12. In part a) is a contour plot for x-polarized input beam, width w × height h = 300 nm x 200 nm. Part b) shows the cross-sections along the x-axis (y=0) and y-axis (x=0) over a larger range to highlight the behavior near the surface of the nanobeam, and over a smaller range highlighting the behavior further away from the nanobeam's surface. In the cross-section plots, there are multiple curves corresponding to varying widths w = 100, 150, 200, 250, 300, 350, 400 nm colored in red, blue, green, magenta, brown, cyan, orange respectively. We note that $w = 300$ nm (brown curve) gives the largest relative atom-photon coupling strength λ^2/A_{eff} at the surface of the nanobeam at $x - w/2 = 0$ (y=0). For $w = 100$ nm and 150 nm, although they have small values of λ^2/A_{eff} near the surface, they have long decay lengths and have larger λ^2/A_{eff} than the wider nanobeams at greater distances away from the surface of the nanobeam. Finally we note that although the general behavior is quite similar between the single nanobeam and the nanofiber discussed in Sec. 3.2.1.2, there are at least three important features that may make the silicon nitride nanobeam preferable. Firstly, in contrast to the circular cross-section nanofiber, the intrinsic rectangular cross-section breaks the azimuthal symmetry and could improve the stability of the polarization direction of the guided mode. Secondly, the lithographically patterned and fabricated silicon nitride nanobeam offers more flexibility and better control in terms of adding features such as photonic crystal mirrors to make a cavity, as well as integrating periodic structure throughout the nano-waveguide to create band-structures. And thirdly, in contrast to nanofibers, it offers the potential to go beyond one-dimensional systems, to two-dimensional architectures.

3.3.2 Double nanobeam

Figure 3.13 a) shows a schematic of a double nanobeam structure, which consists of similar sections to the single nanobeam (butt coupler, large-to-small adiabatic mode converter, and a photonic crystal mirror at the end), but with a modified center section which now may contains a double beam mode selector and double nanobeam waveguide. Starting from the similar single beam structure as discussed in Sec. 3.3.1, we now have a Y-junction that converts the single beam mode to a double beam mode, followed by a double beam mode selector, where the individual beam's width can be different, chosen to potentially induce relative phase-shift between one arm of the double beam relative to the other arm (to allow excitation of even vs odd modes as suggested by Su-Peng Yu), to be then followed by the nanophotonic double beam waveguide. Fig. 3.13 c) shows the double nanobeam waveguide including the coordinates (x, y, z), width w, height h, and gap (e.g., with w = 300 nm, h = 200 nm, and gap = 200 nm).

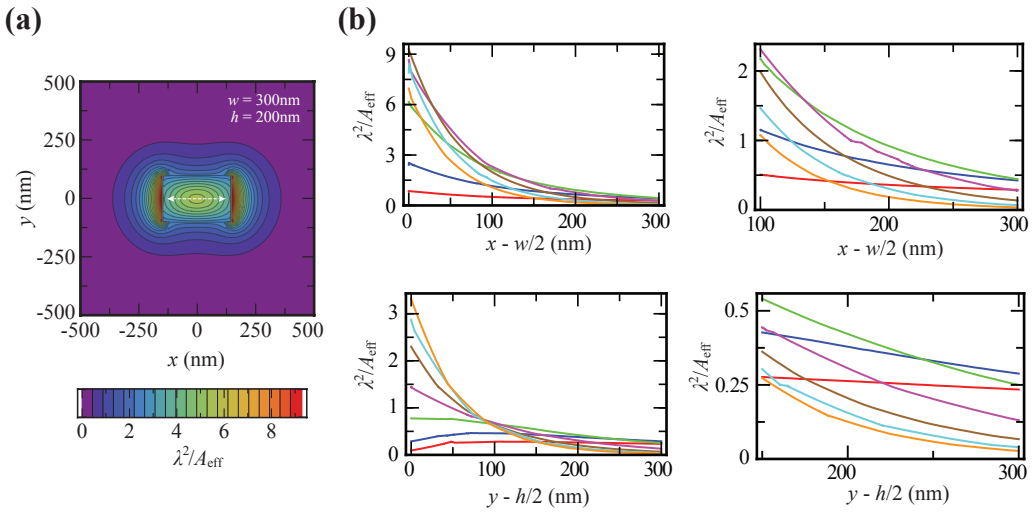

Figure 3.12: **Single nanobeam mode effective area.** Contour and cross-sectional plots of λ^2/A_{eff} showing atom-photon interaction strength profile, for a single nanobeam fundamental x-polarized mode. **a)** The contour plot corresponds to nanobeam with width $w = 300$ nm and height $h = 200$ nm. **b)** For the cross-sectional plots, the curves colored in red, blue, green, magenta, brown, cyan, and orange correspond to single nanobeam with height $h = 200$ nm and width $w = 100$, 150, 200, 250, 300, 350, 400 respectively. Each row in (b) show the same curves, over a different domain. In the first column, the behavior close to the surface is more clearly shown while in the second column, the behavior far from the surface is more clearly displayed.

The 'fundamental' mode of the double beam now consists of the four lowest order modes as the two individual beams are now coupled together. In Fig. 3.13 b), we plot the effective refractive index $n_{\text{eff}} = \beta/k$ where β is the propagation constant of the guided mode and $k = 2\pi/\lambda$ is the propagation constant in free-space or the wavenumber, as a function of V which we define to be $V \equiv k\alpha\sqrt{n^2 - 1}$, where α is set to 200 nm, and $n = 2.0$ is the refractive index of the silicon nitride nanobeam, showing these four lowest order modes. Superimposed are the lines showing the modes at $\lambda = 852, 687, 937$ nm corresponding to cesium D2 line transition wavelength and the blue- and red-detuned magic wavelengths respectively. Here, we see that for $V \lesssim 3$, the double beam support four (lowest order) modes, (i), (ii), (iii), (iv), corresponding to even x-polarized, even y-polarized, odd x-polarized, and odd y-polarized modes respectively, which are ordered from the lowest-order of the four modes to the higher orders. Even and odd modes refer to symmetric and anti-symmetric electric field signs, as shown in Fig. 3.13 d), where the rows (i), (ii), (iii), (iv) correspond to the electric field distributions for the four lowest order modes (i), (ii), (iii), (iv) shown in Fig. 3.13 b). For discussions on the electric field distributions, including the presence of multiple electric field components (E_x, E_y, E_z) including $\pi/2$ out-of-phase E_z component, refer to discussions in Sec. 3.2 and Sec. 3.3.1. We note that for $V > 3$, there exist more than four modes for the double nanobeam

structure we consider (w = 300 nm, h = 200 nm, gap = 200 nm).

As in Sec. 3.3.1, here we show calculation results of λ^2/A_{eff} for a specific double nanobeam structure (w = 300 nm, h = 200 nn, gap = 200 nm) as a contour plot in Fig. 3.14 a), and for varying widths w and gap (keeping h = 200 nm fixed) in parts b), c) and d). In part c), we show the cross-sections of λ^2/A_{eff} along the x axis (at $y = 0$), for $w = 150, 300, 350$ (the three rows), and within each plot, multiple curves for gap =100, 150, 200, 250, 300, 350, 400, 450, 500 nm (i.e., nine curves starting from gap = 100 nm to gap = 500 nm, in steps of 50 nm), with gradient colors from light to dark blue respectively. In part d), we have the same parameter sets for the three rows and nine curves as in part c), except here the cross-section is along the y-axis (at x=0). Finally in part b), are plots of λ^2/A_{eff} as a function of gap parameter (from 100 nm to 500 nm), for the coordinates (x, y) = (0,0), h = 200 nm, and varying widths w = 150, 200, 250, 300, 350 nm corresponding to the red, blue, green, magenta, orange curves respectively. The top of Fig. 3.14 b) highlights the behavior near the small gap region (with linear scaling in λ^2/A_{eff}) whereas the bottom plot highlights the behavior in the large gap region (with logarithmic scaling in λ^2/A_{eff}).

3.3.3 Experiment setup and techniques

Figure 3.15 shows the experimental setup in lab 1 based on the nanophotonic beams and cavities discussed in the previous sections. This is an on-going work performed by many individuals in multiple labs in our group and in Painter group, who I would like to acknowledge here. Firstly, in lab 11: Akihisa Goban and Chen-Lung Hung who first implemented the multi-magneto-optical trap scheme to transport an atomic cloud from the source chamber to the science chamber and into the photonic device chip in our group, which was critical in forming the basis of our setup in lab 1; our collaborator Kyung Soo Choi; Jonathan Hood and Su-Peng Yu who closely worked with device characterization and fabrication; with Sean Meneehan and Richard Norte in Painter group. In lab 2: Jae Hoon Lee, Juan Muniz, and Ding Ding. Last but not least, the team in lab 1 who directly work in the experimental setup discussed in this thesis: Andrew McClung, Pol Forn-Diaz, Martin Pototschnig; I would also like to acknowledge Clement Lacroute from our group; and Justin Cohen, Taofiq Paraiso, and Alex Krause in Painter group. This work is carried out under the guidance and supervision of my advisor, Prof. Jeff Kimble, in collaboration with Prof. Oskar Painter at Caltech.

The heart of our experimental setup is shown in Fig. 3.15 a) and d), and consists of two chambers separated by about 70 cm distance. Starting from the source MOT chamber labeled (i) in part a) of Fig. 3.15, where about $10^7 - 10^8$ atoms are magneto-optically trapped, a near-resonant (e.g., 10 MHz

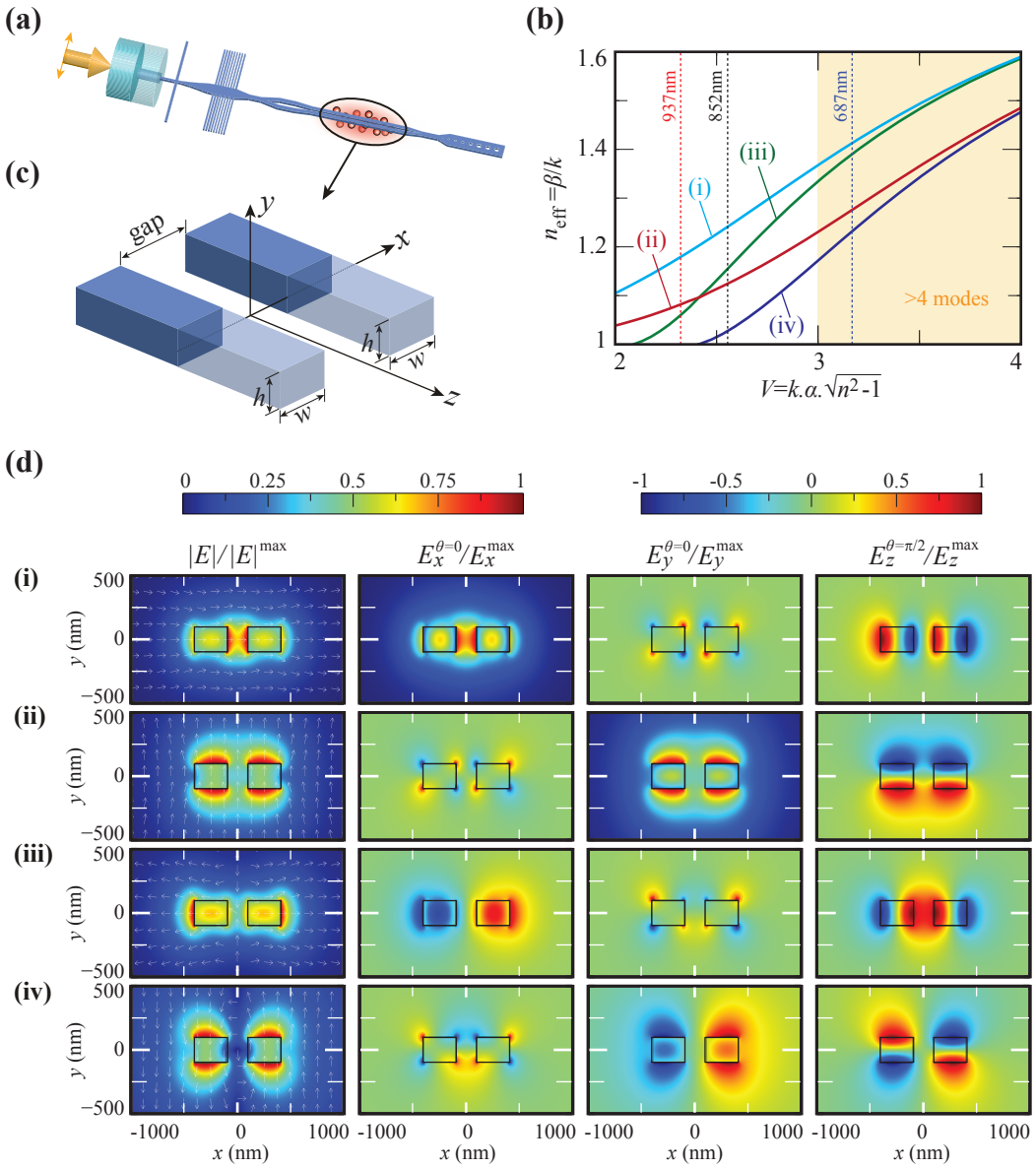

Figure 3.13: **Double nanophotonic beam and mirror. a, c)** Schematic of a double nanobeam device showing optical fiber to silicon nitride waveguide butt-coupling, adiabatic adapter to nanobeam mode, a Y-junction single-to-double beam mode converter, a double nanobeam waveguide with width w, height h, separated by a gap, followed by a photonic crystal mirror. The dimensions are discussed in the text. **b)** Dispersion curves showing effective refractive index $n_{\text{eff}} = \beta/k$ where β = propagation constant of the guided mode, $k = 2\pi/\lambda$ = free-space wave number, $\alpha = 200$ nm and $n = 2.0$, of the first lowest order supermodes, for symmetric (even) modes: x-polarized (i) and y-polarized (ii), and anti-symmetric (odd) modes: x-polarized (iii) and y-polarized (iv). Higher-order modes start to appear beyond $V \simeq 3$ in the shaded region. **c)** Double nanobeam waveguide. **d)** Normalized electric field $|E|$ profiles and the components $\{E_x^\theta, E_y^\theta, E_z^\theta\}$ (where θ indicates the optical phase and location along the z-axis. E.g., $\theta = 0 \leftrightarrow z = 0, \theta = \pi/2 \leftrightarrow z = \lambda/4$) for the double nanobeam ($w = 300$ nm, $h = 200$ nm, gap = 200 nm) four lowest order modes polarized along x. For (i), $E_x^{\max} = 0.920|E|^{\max}, E_y^{\max} = 0.440|E|^{\max}, E_z^{\max} = 0.429|E|^{\max}$. For (ii), $E_x^{\max} = 0.454|E|^{\max}, E_y^{\max} = 0.895|E|^{\max}, E_z^{\max} = 0.469|E|^{\max}$. For (iii), $E_x^{\max} = 0.863|E|^{\max}, E_y^{\max} = 0.445|E|^{\max}, E_z^{\max} = 0.572|E|^{\max}$. For (iv), $E_x^{\max} = 0.498|E|^{\max}, E_y^{\max} = 0.910|E|^{\max}, E_z^{\max} = 0.446|E|^{\max}$.

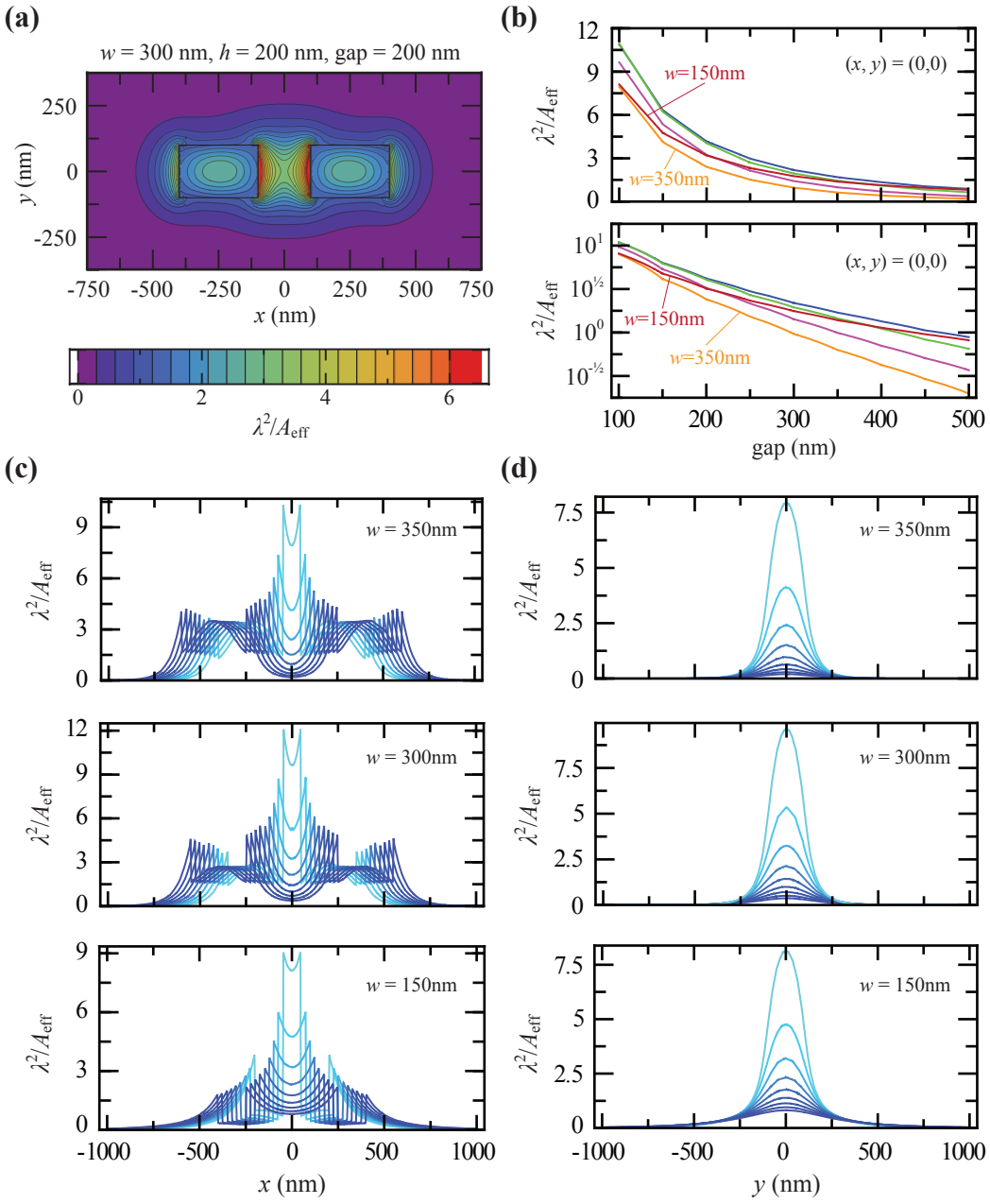

Figure 3.14: **Double nanobeam mode effective area.** Plots of λ^2/A_{eff} showing atom-photon interaction strength profile, for a double nanobeam lowest-order x-polarized (even) mode. **a)** Contour plot corresponds to nanobeam with width $w = 300$ nm, height $h = 200$ nm and gap = 200 nm. **b)** Plot of λ^2/A_{eff} at $\{x, y\} = \{0, 0\}$ as a function of varying gap parameter. The curves colored in red, blue, green, magenta, orange correspond to double nanobeam with height $h = 200$ nm and width $w = 150$, 200, 250, 300, 350 nm respectively. **c-d)** Cross-sectional plots for double nanobeam structure with height $h = 200$ nm, varying widths w as labeled in each panel. For each panel, the gap size is scanned from gap = 100 nm (lightest blue) to gap = 500 nm (darkest blue) in steps of 50 nm. In c), the plots are along x-axis ($y = 0$), and in d), the plots are along y-axis ($x = 0$).

blue-detuned) push beam (with beam diameter ≈ 1 mm, power of ≈ 3 mW, and a slightly diverging profile), indicated by the green arrow in Fig. 3.15 a), pierces through the large MOT cloud, creating a flux of atoms that slowly diverges in the transverse direction due to its temperature, moving towards the science chamber (vi) [241]. The two chambers are separated by an all-metal in-line valve (iii), so that each can be individually isolated and pumped down independently through the all-metal valves (ii) and (iv). In operation, both chambers are continuously kept at UHV by two operating ion pumps, one for the source chamber (not shown) and one for the science chamber (v). The source of Cesium atoms in the MOT chamber is a getter, giving a background pressure of $\sim 10^{-9}$ torr in operation. With no strong differential pumping tube (narrowest tube diameter is about 1 cm), the ≈ 70 cm distance from the source to science chamber, the ≈ 70 cm distance from science chamber to the ion pump (v), and all the vacuum connections, we have a differential pressure factor of ≈ 10 between the source and science chamber. In operation, the science chamber background pressure is $\approx 10^{-10} - 10^{-9}$ torr.

We note that one important parameter in this system is the atom number and density of the atom cloud that can be delivered to the nanophotonic chip in the science chamber. Unlike in the toroid case, where it is not possible to overlap a MOT cloud over the toroid device, here it is actually possible to overlap a MOT cloud directly over the nanophotonic chip's thru-hole, where the nanophotonic devices are located, forming little thin bridges. This offers benefits in terms of size and density of atom cloud, as well as the possibility of cooling the atoms, for example through the simplest Doppler-cooling (optical molasses) of the MOT, and sub-Doppler cooling with polarization-gradient cooling techniques.

The jet of cesium atoms coming from the source chamber to the science chamber is then collected by a large magneto-optical trap (with practically maximized MOT beam diameter of ≈ 2 cm to cover as large as possible capture velocity and to collect as many atoms as possible). Here, we magneto-optically trap $\approx 2 \times 10^7$ atoms (after 1 second loading time), which are then polarization-gradient cooled, and compressed by increasing the detunings of the MOT and repumper beams, and at the same time attenuating the optical powers [58], leading to about a two-fold density increase to $\approx 4 \times 10^{10}$ atoms/cm^3. This dense first MOT in the science chamber is illustrated in the left panel of Fig. 3.15 b), showing the jet of cesium atoms coming from the left (source chamber), magneto-optically trapped by the large X-shaped counter-propagating beams (and also a pair for the vertical confinement): see the red arrows Fig. 3.15 a) representing the three pairs of large MOT beams at the science chamber (vi). An absorption image of this dense MOT is shown in Fig. 3.15 b) panel (i).

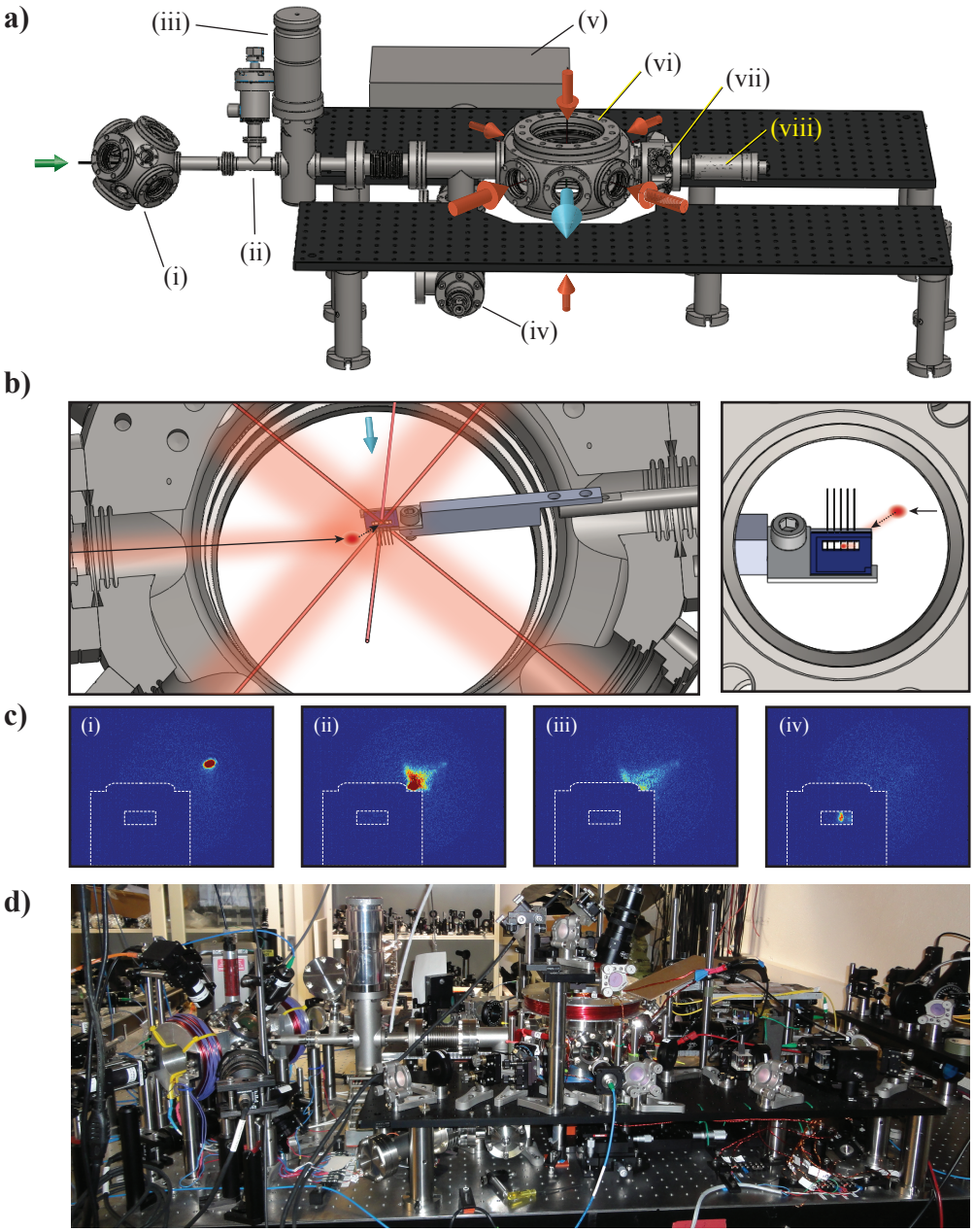

Figure 3.15: **Nanophotonic beams and cavities experiment setup. a)** Schematic of experimental setup showing two chambers separated by 70 cm connected by a differential pumping tube, where a magneto-optically trapped atom cloud is formed in the first chamber (i), pierced through by a near-resonant push beam (green arrow) that forms a jet of atoms, to be captured by a second magneto-optical trap in the science chamber (vi) formed by three pairs of counter-propagating beams shown by the red arrows, and in b). Following this stage, the cloud of atoms in the science chamber is transported and recaptured by a mini-magneto-optical trap inside the chip's thru-hole over the nanophotonic devices, formed by three pairs of small counter-propagating cooling and trapping beams shown in b). The setup is designed with multiple vacuum valves (ii), (iii), (iv) allowing frequent loading/unloading of nanophotonic device chip mounted on a multiplexer (vii) and translation stage (viii). **c)** Fluorescence image showing atom cloud transport from science chamber large MOT to mini-MOT inside the chip, taken with CCD camera with viewing direction shown by the cyan arrow in a) and b), also shown on the right panel of b). **d)** Setup built for our experiment.

At this stage, we have a nice dense MOT cloud in the science chamber, but it is not yet positioned to overlap the nanophotonic device on the chip. The final step involves transporting this MOT cloud by changing the zero-field location of the quadrupole field (by changing the three pairs of bias-coils), so that the new zero is located right inside the thru-hole of the nanophotonic chip, where another independent setup of three pairs of counter-propagating MOT beams, called mini-MOT beams to distinguish from the large MOT beams we discussed above, form a mini-MOT at the center of the nanophotonic chip. These mini-MOT beams have beam diameter in the order of ≈ 1 mm, fitting in nicely with the chip's through-hole opening of 2 mm x 6 mm. More detailed mechanism of this MOT transport will be discussed in Chapter 8 and can also be found in Chapter 5 of [221]. We note that due to the mechanism that involves atom velocity-selection coupled to the magnetic field profiles or directions, the transport is quantized and is only efficient over certain directions with respect to the magnetic field distribution [218, 242, 221]. With this technique, we could transport the first MOT cloud to the second mini-MOT location over ≈ 1 cm in ≈ 10 ms, with about 50% transport efficiency. This leads to a mini-MOT cloud positioned overlaping a nanophotonic device (inside the chip's thru-hole), with atom number of $\approx 7 \times 10^6$ atoms with a density of 10^{10} atoms/cm^3. Figure 3.15 c) shows a time-series in panels (i) to (iv) measuring the transport of the MOT cloud within the science chamber, from the first large MOT (i) to the mini-MOT (iv) inside the nanophotonic chip. These images show absorption by the atom cloud of a resonant weak beam shone towards the CCD camera; note that the shadow of the nanophotonic chip with its through-hole structure is also visible. These images were taken with a side-view CCD camera, facing the direction shown by the cyan arrow in Fig. 3.15 a) and b). The right hand panel of Fig. 3.15 b) shows the view of the CCD camera, with the MOT transports indicated by the arrows. The dotted arrows showing the MOT transport to the mini-MOT indicate that the atom cloud goes behind the chip as seen from the CCD camera.

Finally we note that the chip is mounted on a translation stage with axial linear tunability and rotational tunability (labeled by (viii) in Fig. 3.15 a)). The translation stage is connected to a multiplexer (vii) with optical fiber feed-throughs, which is connected to the science chamber. For more detailed discussion on the experimental setup and schemes, please refer to Chapter 8.

3.4 Summary

In this chapter, we have presented an overview of the three platforms considered in this thesis, namely: microtoroidal cavity QED where we realized an efficient single photon router [10] and observed in real-time strong-coupling of single cesium atoms to single photons in the whispering

gallery mode of an on-chip microtoroid resonator [5]; a tapered optical nanofiber where significant atom-photon coupling through absorption spectroscopy has been observed [91] via state insensitive trapping of single atoms $\sim$ 210 nm close to the surface of a nanofiber; and finally a nanophotonic waveguide where techniques from the earlier platforms are being combined for promising prospects of achieving very strong atom-photon coupling and long interaction time through robust atom trapping, as well as possible future exploitation of band-structure effects and many-body physics [40, 41]. These advances help to provide a path towards a full chip-integrated architecture to realize quantum network systems for the realization of quantum networks [132]. More detailed discussions, including the experiments performed and theoretical investigations are presented in the subsequent chapters.